

Nonlinear Parker Instability of Isolated Magnetic Flux  
in a Plasma

K. SHIBATA,<sup>1,2</sup> T. TAJIMA,<sup>1</sup> R. MATSUMOTO,<sup>3</sup>  
T. HORIUCHI,<sup>3†</sup> T. HANAWA,<sup>4,5</sup> R. ROSNER,<sup>6</sup> Y. UCHIDA<sup>7</sup>

August 1988

<sup>1</sup>Department of Physics, University of Texas at Austin

<sup>2</sup>Department of Earth Sciences, Aichi University of Education

<sup>3</sup>Department of Astronomy, University of Kyoto

<sup>4</sup>Max-Planck Institute für Astrophysik

<sup>5</sup>Department of Physics, Nagoya University

<sup>6</sup>Department of Astronomy and Astrophysics, University of Chicago

<sup>7</sup>Department of Astronomy, University of Tokyo

<sup>†</sup>Deceased 1987 June 26

## ABSTRACT

The nonlinear evolution of the 'Parker instability' in an isolated horizontal magnetic flux sheet imbedded in a two-temperature-layered atmosphere is studied by using a two-dimensional MHD code. In the solar case, this two-layer model is regarded as a simplified abstraction of the Sun's photosphere/chromosphere and its overlying much hotter (coronal) envelope. The horizontal flux sheet is initially located in the lower temperature atmosphere so as to satisfy magnetostatic equilibrium under a constant gravitational acceleration. Ideal MHD is assumed and only perturbations with  $k$  parallel to the magnetic field lines are investigated. As the instability develops, the gas slides down the expanding loop, and the evacuated loop rises due to enhanced magnetic buoyancy. In the nonlinear regime of the instability, both the rise velocity of a magnetic loop and the local Alfvén velocity at the top of the loop increase linearly with height and show self-similar behavior with height as long as the wavelength of the initial perturbation is much smaller than the horizontal size of the computing domain. The self-similar acceleration of the rising loop continues as long as the loop is in the low temperature atmosphere. After the loop reaches the higher temperature layer, the acceleration of the rising loop decreases, and eventually the loop decelerates. We have studied this self-similar expanding motion of the magnetic loop analytically, and find that there is a quasi one-dimensional similarity solution for the ver-

tical variation of physical quantities at the mid-point of the magnetic loop. Application to emerging magnetic flux in the solar atmosphere and to other related astrophysical phenomena are also briefly discussed. Similarity to the ballooning mode is mentioned.

## I. Introduction

It has been suggested that much of the 'activity' observed in various astrophysical plasmas may be due to strong magnetic fields (Parker 1979). For example, almost all active phenomena on the Sun (e.g. flares, prominences, corona, jets and/or mass ejections) are caused by strong magnetic fields (e.g. Priest 1981). Activity seen in some stars (X-ray emitting stars, or stellar coronae [Rosner et al. 1985], and flare stars [Byrne and Rodono 1983]) are probably related to strong magnetic fields (Uchida 1986). Magnetic fields may also play an important role in galactic disks (Sofue *et al.* 1986, Sawa and Fujimoto 1986, Fujimoto and Sawa 1987, Asseo and Sol 1987), accretion disks (Galeev *et al.* 1978, Takahara 1979, Stella and Rosner 1983, Kato and Horiuchi 1984, 1985), and cosmic jet phenomena (e.g. Uchida and Shibata, 1985, 1986, Shibata and Uchida, 1985, 1986).

Magnetic buoyancy plays a major role in the occurrence of these various magnetic phenomena (Parker 1955, 1979) because the magnetic fields created by dynamo action are transported from the interior of celestial bodies to their surface by magnetic buoyancy. Similarly, it may play an important role in star formation by allowing the magnetic field to escape. The 'Parker instability' (Parker 1966, 1969, 1979) is a kind of ideal magnetohydrodynamic instability driven by such magnetic buoyancy, and is related to the magnetic Rayleigh-Taylor instability. In a narrow sense, the magnetic Rayleigh-Taylor instability (Kruskal and Schwarzschild 1954) is an interchange (or flute) in-

stability which occurs for perturbations with  $\mathbf{k} \perp \mathbf{B}$  and  $\mathbf{k} \perp \mathbf{g}$  where  $\mathbf{k}$  is the wavenumber vector, and  $\mathbf{B}$  and  $\mathbf{g}$  are the magnetic field and gravitational acceleration vectors. On the other hand, the Parker instability occurs for long-wavelength perturbations with  $\mathbf{k} \parallel \mathbf{B}$  (i.e. undular mode) even when the system is stable against the interchange mode perturbations (Newcomb 1961).

In this sense, the Parker instability is similar to the ballooning instability in fusion plasmas (Bateman 1978). It is known that the ballooning instability sets the largest achievable plasma  $\beta$  (= the ratio of gas to magnetic pressure), the critical  $\beta$ , in a Tokamak or other toroidal confinement devices. Thus, it is important to understand the physical nature of the ballooning instability. Although a large number of linear analyses exists, few numerical simulations of its nonlinear evolution have been carried out to date to our best knowledge (Ogino *et al.* 1981, Brunel *et al.* 1981). This is perhaps because in fusion research the linear theory determines the critical  $\beta$  which proves to be a reliable predictor of the experimentally observed critical  $\beta$ . In these experiments, once linear instabilities set in, they generally do not saturate and in fact continue to grow nonlinearly (as we shall see in this paper), and thus the plasma containment eventually is defeated.

The effective gravity in the ballooning instability comes from the "bad" curvature of magnetic field lines, or equivalently, from the centrifugal acceleration of charged particles moving along curved magnetic field lines. Thus,

the 'gravitational force' acts outward in a Tokamak. Since the particle number density is larger within the Tokamak than in the outer region, it can be said that heavy gas is situated at higher gravitational potential in the Tokamak. This situation is different from that of the gas layer considered in this paper, in which the density is smaller at higher gravitational potential. This is because in many man-made confinement devices it is often topologically unavoidable to have a "bad" curvature region where denser matter is in the higher potential, while in natural gravitational settings, the natural equilibrium is such that the opposite is the case. If one looks at the magnetic buoyancy instability locally, however, there exists in fact a region where denser matter is in the higher gravitational potential, i.e., just above the magnetic flux. In spite of this difference, the results in the present paper may prove to be useful to the exploration of nonlinear properties of the ballooning instability.

Parker (1966) originally proposed the undulation (Parker) instability to explain the formation of interstellar clouds (Shu 1974, Mouschovias 1974, Mouschovias *et al.* 1974, Zweibel and Kuksrud 1975, Asseo *et al.* 1979, Elmegreen 1982), but the physics involved is closely related to the rise and emergence of the magnetic flux tubes in the Sun and stars as well (Acheson 1979, Schüssler 1980, Spruit and van Ballegoijen 1982, Schmitt and Rosner 1983, Moreno-Insertis 1986, Hughes and Proctor 1988). (As for other astrophysical applications of the Parker instability, see e.g. Piddington 1970,

Sofue 1973, Tosa and Sofue 1974, Baierlein *et al.* 1981, Duric *et al.* 1983.)

Recently, Matsumoto *et al.* (1988) have studied the nonlinear time evolution of the Parker instability (Parker 1966) for a magnetostatic gas layer in a non-uniform gravitational field. Taking two-dimensional Cartesian coordinates  $(x, z)$ , they assumed that the gravitational acceleration vector is parallel to the  $z$ -direction and anti-symmetric with respect to  $z = 0$ , and that its magnitude is independent of  $x$  and has the same  $z$ -dependence as that of  $z$ -component of gravity at a point  $x \neq 0$  and  $y \neq 0$  in a spherically symmetric potential produced by a point mass at  $x = y = z = 0$ . Initial magnetic fields were taken to be parallel to the  $x$ -direction, i.e. vertical to the gravity. Such gas layers may be a model for the local part of magnetized gas layers around the equatorial plane in accretion disks and/or galactic disks. They considered only isothermal perturbations in the initial gas disk, with constant Alfven and sound speeds. Their main results are as follows. As the instability develops, the gas slides down the expanding loop, forming dense clouds in the valleys, with rarefied loops between. The expansion of the loop is decelerated when the maximum velocity of the downflow becomes comparable to or larger than the initial Alfven speed. Shock waves are produced in the downflow when the initial Alfven speed is larger than the sound speed. The maximum rise velocity of the loop is about 0.3 - 0.4 times that of the initial Alfven speed. The reason why the expanding motion of the loop is decelerated is that the gravitational acceleration decreases with height in this

model; i.e. the magnetic loop penetrates into the Parker-stable region (small  $g$  region) in the nonlinear regime.

The purpose of this paper is to extend the work by Matsumoto *et al.* (1988) to the situation suitable for the Sun and stars and to extract the general characteristics of the undulation (Parker) instability in the nonlinear stage. We will study the nonlinear evolution of the Parker instability of an isolated magnetic flux sheet imbedded in a two-temperature layered atmosphere, such as the solar corona-chromosphere/photosphere system, stratified under a constant gravitational acceleration. Isolated magnetic flux tubes are observed in the solar photosphere, and are suggested to exist also in the solar convection zone (e.g. Zwaan 1987). Physically, the isolation of magnetic flux into tubes implies that the instability develops within a finite region; this contrasts with the model first considered by Parker (1966), i.e. a magnetostatic gas layer with constant Alfvén and sound speeds under constant gravitational acceleration, where instability occurs in an infinite space, or in other words, the velocity eigenfunction increases exponentially with height. Because of various constraints on numerical simulations, we consider only a two-dimensional (2D) flux sheet. Thus, the interchange mode (perturbation with  $\mathbf{k} \perp \mathbf{B}$  and  $\mathbf{k} \perp \mathbf{g}$ ) will not be studied in this work (Hughes and Cattaneo 1987). The different functional form of the gravitational acceleration considered here from that of Matsumoto *et al.* (1988) allows to study how the nonlinear evolution of magnetic loop expansion occurs when the loop



rises through Parker-unstable layers.

§II describes the assumptions and basic equations, and §III presents numerical results. In §IV, we study the quasi 1D self-similar solution for this problem by analytical methods. According to these analytical solutions, we could understand physics of our complex numerical results. In fact, the analytical formula for the distribution of density and magnetic field in equation (15) and (16) were first derived by this quasi 1D theory. Finally, §V is devoted to the summary and discussions. Appendix A summarizes the main characteristics of linear stability for the gas layer considered in the present paper. In Appendix B, we investigate other self-similar solutions of the quasi-1D MHD equation used in §IV for the case of  $\lambda \ll X_{max}$ , where  $\lambda$  is the horizontal wavelength in the initial perturbation, and  $X_{max}$  is the horizontal size of the computing domain. These solutions are useful to understand the physical meaning of the particular self-similar solution obtained in §IV.

## II. Basic Equations and Numerical Methods

### a) Assumptions and Basic Equations

We assume the following: (1) the medium is an ideal gas, (2) the gas is a polytrope of index  $\gamma = 1.05$  (recall that the larger  $\gamma$  is, the larger is the computational time [Parker 1979, Matsumoto and Horiuchi 1988]; hence, this value of  $\gamma$  is chosen simply for computational convenience), (3) the magnetic field is frozen into the gas, (4) the gravitational acceleration is constant, (5) only two-dimensional motion are allowed. Cartesian coordinates  $(x, y, z)$  are adopted so that the  $z$ -direction is anti-parallel to the gravitational acceleration vector. It is assumed that  $V_y, B_y$ , and  $\partial/\partial y$  are all zero. Thus, the basic equations in scalar form are as follows:

$$\frac{\partial \rho}{\partial t} + \frac{\partial}{\partial x}(\rho V_x) + \frac{\partial}{\partial z}(\rho V_z) = 0, \quad (1)$$

$$\frac{\partial}{\partial t}(\rho V_x) + \frac{\partial}{\partial x}[\rho V_x^2 + p + \frac{1}{8\pi}(B_z^2 - B_x^2)] + \frac{\partial}{\partial z}(\rho V_x V_z - \frac{1}{4\pi}B_x B_z) = 0, \quad (2)$$

$$\frac{\partial}{\partial t}(\rho V_z) + \frac{\partial}{\partial x}(\rho V_x V_z - \frac{1}{4\pi}B_x B_z) + \frac{\partial}{\partial z}[\rho V_z^2 + p + \frac{1}{8\pi}(B_x^2 - B_z^2)] + \rho g = 0, \quad (3)$$

$$\frac{\partial}{\partial t}B_x + \frac{\partial}{\partial z}(V_z B_x - V_x B_z) = 0, \quad (4)$$

$$\frac{\partial}{\partial t}B_z - \frac{\partial}{\partial x}(V_z B_x - V_x B_z) = 0, \quad (5)$$

$$\frac{\partial}{\partial t}[\frac{p}{\gamma - 1} + \frac{1}{2}\rho(V_x^2 + V_z^2) + \frac{1}{8\pi}(B_x^2 + B_z^2)]$$

$$\begin{aligned}
& + \frac{\partial}{\partial x} \left[ \frac{\gamma}{\gamma-1} p V_x + \frac{1}{2} \rho V_x (V_x^2 + V_z^2) + \frac{B_z}{4\pi} (V_x B_z - V_z B_x) \right] \\
& + \frac{\partial}{\partial z} \left[ \frac{\gamma}{\gamma-1} p V_z + \frac{1}{2} \rho V_z (V_x^2 + V_z^2) + \frac{B_x}{4\pi} (V_z B_x - V_x B_z) \right] + \rho g V_z = 0, \quad (6)
\end{aligned}$$

where  $g$  is the gravitational acceleration, and other symbols have their usual meaning.

## b) Initial Conditions

### i) Equilibrium State

We consider a two-temperature-layered atmosphere similar to the solar corona-chromosphere/photosphere system. Hereinafter, we call the lower temperature atmosphere simply the chromosphere, and the higher temperature atmosphere the corona, although the application is not restricted only to the Sun. The distribution of the initial temperature is assumed to be

$$T(z) = T_{ch} + (T_{cor} - T_{ch}) \frac{1}{2} \left[ \tanh\left(\frac{z - Z_{cor}}{w_{tr}}\right) + 1 \right], \quad (7)$$

where  $T_{cor}/T_{ch}$  is the ratio of the temperature in the corona to that in the chromosphere,  $Z_{cor}$  is the height of the base of the corona,  $w_{tr}$  is the temperature scale height in the transition region ( $= 0.6H$  for all our calculation, where  $H$  is the pressure scale height of the chromosphere). We have calculated both cases of  $T_{cor}/T_{ch}=100$  and 25 in some typical models, and found

that the results in both cases are very similar. Thus, we will show only the results with  $T_{cor}/T_{ch} = 25$  in the following sections:

We assume that the magnetic field is initially parallel to the  $x$ -axis;  $\mathbf{B} = (B(z), 0, 0)$ , and is localized in the chromosphere. The distribution of magnetic field strength  $B(z)$  is given by

$$B(z) = [8\pi p(z)/\beta(z)]^{1/2},$$

where

$$\beta(z) = \beta_*/f(z), \quad (8)$$

$$f(z) = \frac{1}{4}[\tanh(\frac{z-z_0}{w_0}) + 1][-\tanh(\frac{z-z_1}{w_1}) + 1],$$

and where  $\beta_*$  is the ratio of gas pressure to magnetic pressure at the center of the magnetic flux sheet,  $z_0$  and  $z_1 = z_0 + D$  are the heights of the lower and upper boundary of the magnetic flux sheet, and  $D$  is the vertical thickness of the magnetic flux sheet. It is assumed that  $z_0 = 4H$ ,  $D = 4H$ ,  $w_0 = w_1 = 0.5H$  for all of our calculations.

The initial density and pressure distributions are numerically calculated by using equations (7), (8) and the equation of magneto-static balance

$$\frac{d}{dz} \left[ p + \frac{B^2(z)}{8\pi} \right] + \rho g = 0. \quad (9)$$

## ii) Perturbations

Small velocity perturbations of the form

$$V_x = f(z)AC_s \sin\left[\frac{2\pi(x - X_{max}/2)}{\lambda}\right], \quad (10)$$

are initially imposed on the magnetic flux sheet ( $z_0 < z < z_1$ ) within the finite horizontal domain ( $X_{max}/2 - \lambda/2 < x < X_{max}/2 + \lambda/2$ ), where  $\lambda$  is the horizontal wavelength of the small velocity perturbation,  $X_{max}$  is the horizontal size of the computing domain, and  $A$  is the maximum value of  $V_x/C_s$  in the initial perturbation ( $=0.05$ ). This perturbation is not exactly the same as one of the unstable eigenfunction. However, the eigenfunction is numerically determined, and the growth rate of the perturbation in the linear regime agrees well with that obtained from the exact linear analysis (Appendix A; see also Horiuchi et al. 1988, Matsumoto and Horiuchi 1988).

### c) Boundary Conditions and Numerical Procedures

We assume periodic boundaries for  $x = 0$  and  $x = X_{max}$ , a symmetric (rigid conducting wall) boundary for  $z = 0$ , and a free boundary for  $z = Z_{max}$  (see for example Shibata [1983]). The effect of the free boundary at  $z = Z_{max}$  is small.

Equations (1)–(6) are non-dimensionalized by using the following normalizing constants:  $H$  (the scale height of the chromosphere),  $C_s$  (the sound velocity in the chromosphere), and  $\rho_0$  (the density at the base of the atmosphere,  $z = 0$ ). The units of length, time, and velocity are  $H$ ,  $H/C_s$ ,  $C_s$ . The

gas pressure, density and magnetic field strength are normalized by  $\rho_0 C_s^2$ ,  $\rho_0$ , and  $(\rho_0 C_s^2)^{1/2}$ , respectively. Equations (1)–(6) are then solved numerically by using a modified Lax-Wendroff scheme (Rubin and Burstein 1967) with artificial viscosity (Richtmyer and Morton 1967).

The mesh sizes are  $\Delta z = 0.15$  or  $0.1$  for  $z < Z_{cor}$  and slowly increasing for  $z \geq Z_{cor}$ ,  $\Delta x = X_{max}/(N_x - 1)$ , where  $N_x$  is the number of mesh points in the  $x$ -direction. The total number of mesh points is  $(N_x \times N_z) = (81 \times 172)$  in the case of models 1 and 2, and  $(N_x \times N_z) = (101 \times 172)$  in models 3–8. The total area in a typical case (model 1) is  $(X_{max} \times Z_{max}) = (20 \times 35)$ .

The tests and the accuracy of the MHD code have been described in Shibata (1983), Shibata and Uchida (1985), Matsumoto et al. (1988) and Umemura *et al.* (1988). Conservation of total mass and total energy obtains within one percent of their initial values for all models described in this paper.

### III. Numerical Results

#### a) The case of $\lambda = X_{max}$ (Model 1) : Bubble-like Expansion

In this subsection, we show the results in model 1 which is a typical case for  $\lambda = X_{max}$ . The parameters of this model are as follows:  $\beta_* = 1$ ,  $\lambda = 20 = X_{max}$ , and  $Z_{cor} = 18$ . This horizontal wavelength ( $\lambda=20$ ) is close to the wavelength for the maximum growth rate for  $\beta_*=1$ , and the growth rate is 0.121 in the unit of  $C_s/H$  (see Appendix A).

#### i) Overall Evolution

Figure 1 shows the time variations of the magnetic lines of force  $\mathbf{B} = (B_x, B_z)$ , the velocity field  $\mathbf{V} = (V_x, V_z)$ , and the density distribution ( $\log \rho$ ). The instability grows with the characteristics of linear instability up to about  $t = 35$ . Since the density distribution has a steep gradient along the  $z$ -direction, the small perturbation grows to large amplitude when the disturbance propagates from the magnetic flux sheet region to the upper atmosphere. Thus, at  $t = 31.3$ , we see a large velocity pattern around the interface between the corona and the chromosphere, which is possibly the manifestation of the surface wave on the interface. The velocity pattern inherent in the Parker instability is seen around the magnetic flux sheet, in the expansion of the loop and in the downflow along the loop. The dense

regions are created in the valleys of the undulating field lines, whereas the rarefied regions are produced around the tops of magnetic loops. These characteristics are the same as in the nonlinear Parker instability in a non-uniform gravitational field (Matsumoto *et al.* 1988). At this time ( $t = 31.3$ ), the velocities of the rising loop and the downflow are about 0.5 and 1.0 in the unit of the initial sound speed in the chromosphere.

---

Figure 1

---

The rise velocity of the magnetic loop increases as it moves to higher altitudes. At  $t = 41.9$ , the top of the magnetic loop reaches the base of the corona, and the rise velocity of the loop is about 1.1, while the downflow velocity is 2.0; shock waves are produced in the downflow near the footpoints of the loop because the downflow velocity exceeds the local sound speed. After the loop reaches the corona, the upward acceleration of the loop weakens, and eventually the loop is decelerated. At  $t = 47.4$ , the maximum rise velocity of the loop decreases to about 0.6.

It should be noted that a neutral sheet (current sheet) is created just above the valleys of the undulating field lines. Thus, Figure 1c shows at  $t = 41.9$  and 47.4 that in the neutral sheet, the density is enhanced by about a factor 10 when compared with that of the ambient density. Since our model does not include a large resistivity and shear, magnetic reconnection does



not occur. Thus, the neutral sheet survives beyond  $t = 47.4$ . The effects of a large resistivity and magnetic shear should be investigated in the future.

Figures 2a and 2b show the one-dimensional  $z$ -distribution of the vertical velocity ( $V_z$ ) and the density at  $x = X_{max}/2$  (middle of the magnetic loop). The velocity figure (Fig. 2a) clearly shows the acceleration of the rise motion of the magnetic loop in the chromosphere ( $t < 39.9$ ) and its deceleration in the corona ( $t \sim 45.8$ ).

---

Figure 2

---

Figures 2c and 2d shows the  $z$ -distribution of the local Alfvén speed ( $V_A$ ) and the magnetic field strength ( $B_x$ ) at  $x = X_{max}/2$ . As the loop rises, the local Alfvén speed increases due to the evacuation by the downflow along the loop, and hence the local  $\beta$  (not shown here) decreases significantly. (Note that  $\beta \simeq (C_s/V_A)^2$  and  $C_s \simeq \text{constant}$  because of  $\gamma = 1.05$ .)

ii) Why does the Loop Accelerate in the Chromosphere, and Decelerate in the Corona ?

We can simply understand the acceleration of the rise motion of the loop in the chromosphere because the loop is unstable for the undulating perturbation as long as the loop is in the chromosphere. In other words, the restoring magnetic curvature force is still smaller than the accelerating magnetic buoyancy force (or magnetic pressure gradient force) even in the nonlinear stage.

On the other hand, the reason why the rise motion of the loop is decelerated in the corona is that the corona is stable against the horizontal perturbation for wavelengths examined here; the magnetic curvature force is larger than the magnetic buoyancy force in the corona due to the fixed (small) horizontal wavelength. Hence, we suppose that if the wavelength of the magnetic loop increases in the corona, the deceleration of the loop may weaken. This problem will be studied in the next subsection.

Although this intuitive interpretation about the acceleration and deceleration of the loop is correct, the actual force relation is more subtle. We see from Figure 2d that the magnetic field strength ( $B_x$ ) decreases exponentially with height. The approximate relation in the numerical results, shown by the dashed line in Figure 2d, is

$$B_x \propto \exp(-\Delta z/H_m) \quad (11)$$

and  $H_m \simeq 6.4H$ . This relation is the same as that of the potential field found by Parker (1975) for the equilibrium field after the Parker instability occurs. This potential field has the following form:

$$B_x = B_0 \cos\left(\frac{\pi \Delta x}{2L}\right) \exp\left(-\frac{\pi \Delta z}{2L}\right), \quad (12a)$$

$$B_z = B_0 \sin\left(\frac{\pi \Delta x}{2L}\right) \exp\left(-\frac{\pi \Delta z}{2L}\right), \quad (12b)$$

where  $\Delta z = z - z_0$ ,  $\Delta x = x - X_{max}/2$ ,  $2L$  is the horizontal distance between grids of slender rods (line currents) (Parker 1979, p.345, equation [13.77]). Since  $2L$  is equal to  $\lambda$  here, we have  $H_m = 2L/\pi = \lambda/\pi = 20H/\pi \simeq 6.4H$ ,

which agrees with our numerical results. In conclusion, we find that the magnetic field is nearly current free (and thus force free) near the midpoint of the loop, so that the magnetic pressure force approximately balances the magnetic curvature force for all times except for initial short periods. In the accelerating stage ( $t < 40$ ), the magnetic pressure force is a little bit larger than the curvature force, because the top of the loop expands freely in the chromosphere. On the other hand, after the loop enters the corona ( $t > 40$ ), the magnetic pressure finally balances the coronal gas pressure, because the magnetic pressure steeply decreases as  $p_m = B_x^2/8\pi \propto \exp(-2z/H_m)$  and the gas pressure ( $p_g$ ) is nearly constant in the corona (see Fig. 3). Thus, the top of the loop decelerates in the corona, which makes the curvature force slightly larger than the magnetic pressure force even in the chromosphere, leading to the deceleration of the rise motion of the entire magnetic loops.

---

Figure 3

---

## b) The Cases of $\lambda < X_{max}$ : Self-Similar Expansion

### i) The Case of $X_{max} = 2\lambda = 40$ : Model 2

We now study the case of  $\lambda < X_{max}$ , where the effective horizontal wavelength of the loop can increase with time. Figure 4 shows model 2, whose

perturbation wavelength is the same as that of model 1, but the horizontal computing domain is doubled. Other parameters are the same as in model 1. This model is thus equivalent to a model in which both horizontal periodic boundaries are moved away from their original position (model 1) by  $\lambda/2$ . Although the initial perturbation is restricted in horizontal space ( $X_{max}/2 - \lambda/2 < x < X_{max}/2 + \lambda/2$ ), the initially unperturbed part of the magnetic flux sheet is also disturbed by the influence of the instability in the perturbed part. Thus, the magnetic flux in the initially unperturbed part also expands due to the Parker instability, though the onset of the instability occurs later than in the initially perturbed part. Consequently, field lines show the undulating pattern which is more pronounced in the perturbed part than in the unperturbed parts at  $t = 30.6$ .

---

Figure 4

---

The difference between the growth of the instability in the perturbed and the unperturbed parts becomes more significant as time proceeds. At  $t = 41.8$ , the expansion of the magnetic loop in the unperturbed part is almost stopped by the lateral expansion of the magnetic flux in the perturbed part. The magnetic loop in the unperturbed part is significantly compressed at  $t = 49.7$ . The neutral sheet is formed just above the compressed magnetic loop and shock waves are produced in the downflow near the neutral sheet.

The magnetic loop in the initially perturbed part expands very quickly, and the effective wavelength increases with time. Thus, the downflow velocity is larger than in model 1 and equals 2.8 at  $t = 49.7$ . The evolution of the rising loop after entering the corona is also different from that of model 1. Figure 5 shows the  $z$ -distribution of  $V_z$  at  $x = X_{max}$  (the middle of the loop) at various times. It is seen that the rise velocity of the magnetic loop increases even after the loop height exceeds the initial coronal base height, and shows approximate self-similar behavior with height. This is probably because the magnetic curvature force is smaller in model 2 than in model 1 due to the larger effective wavelength.

---

Figure 5

---

## ii) The Case of $X_{max} = 4\lambda = 80$ : Model 3

Figure 6 shows the results for model 3, where the horizontal computing domain is further enlarged ( $X_{max} = 80$ ), with other parameters again fixed as for model 1. In this case, there are four loops (one biggest, two intermediate, and one smallest loops) whose wavelength is approximately the same as  $\lambda$ . The loop formed in the initially perturbed part, which we refer to as the major loop, dominates the other three loops. However, even at  $t = 51.4$ , the major loops do not contact one another. The effective wavelength of

the major loop becomes larger than the wavelength of the dominant loop of model 2, so that the downflow velocity is even larger than in model 2; the maximum downflow velocity at  $t = 51.4$  is about 3.8.

---

Figure 6

---

Figures 7a and 7b show the  $z$ -distributions of  $V_z$  and  $V_A$  at  $x = X_{max}/2$  in model 3, respectively. We find that  $V_z$  and  $V_A$  show self-similar evolution with height. It is also found that (1)  $V_z$  and  $V_A$  increase linearly with height in the chromosphere;

$$V_z(z) = a_1 \Delta z, \quad (13)$$

$$V_A(z) = a_2 \Delta z, \quad (14)$$

where  $\Delta z = z - z_0$ ,  $a_1 = 0.062$ ,  $a_2 = 0.30$ , and  $z_0 = 4$ , (2)  $V_z/V_A = a_1/a_2$  is about 0.2, (3)  $V_z$  increases even after the loop enters the coronal region, though the rate of increase of  $V_z$  in the corona is smaller than in the chromosphere.

---

Figure 7

---

Figures 7c and 7d show the  $z$ -distribution of the density ( $\rho$ ) and the magnetic field strength ( $B_x$ ) at  $x = X_{max}/2$  in model 3. It is seen that the

density and the magnetic field distributions below the top of the loop tends to the steady state distributions with

$$\rho \propto \Delta z^{-4}, \quad (15)$$

and

$$B_x \propto \Delta z^{-1}. \quad (16)$$

This magnetic field distribution is different from the exponential distribution (cf. eq. [11]) for the case of  $\lambda = X_{max}$  because the effective wavelength of the loop increases with height in this case. However, this distribution is again related to the current free (force free) one,

$$B_x \propto \Delta z / (\Delta x^2 + \Delta z^2), \quad (17a)$$

$$B_z \propto -\Delta x / (\Delta x^2 + \Delta z^2). \quad (17b)$$

For this potential field, we have  $B_x \propto \Delta z^{-1}$  for  $|\Delta x| \ll |\Delta z|$ , which agrees with our numerical results.

### iii) Effect of Corona : Models 4 and 5

We now examine the effect of the height of the coronal base,  $Z_{cor}$  (models 4 and 5). As seen in previous sections, the corona has a stabilizing effect on the rising motion of the magnetic loop. Therefore, if  $Z_{cor}$  is larger (smaller), we expect the rise velocity of the magnetic loop to become larger (smaller).

Figure 8 shows the results for model 4, where only  $Z_{cor}$  is changed from a value of 18 (model 3) to 15, with other parameters fixed. We see that the size of the loop (in the density figure of Fig. 8) and the velocities at  $t = 51.5$  are somewhat smaller than those at  $t = 51.4$  in model 3 (Fig. 9). This is due to the smaller value of  $Z_{cor}$ . Figure 9 shows the results for model 5, for which  $Z_{cor} = 12$  and other parameters are the same as in models 3 and 4. It is apparent that the rising motion of the loop is stabilized by the corona. Figure 10 shows the  $z$ -distribution of  $V_z$  at  $x = X_{max}/2$  in models 3, 4 and 5. From this figure we find that the maximum velocity of model 4 ( $= 1.05$ ) is smaller than that of model 3 ( $= 1.4$ ) and that the rise velocity of the loop is decelerated for values of  $z$  larger than  $z = 27$ . We find also that in model 5 ( $Z_{cor} = 12$ ) the acceleration of the rising motion of the loop ceases in the corona for heights larger than 15.

---

Figure 8

Figure 9

Figure 10

---

Figure 11 shows the  $z$ -distribution of the initial gas pressure distribution for models 3, 4 and 5, and the steady magnetic pressure distribution ( $p_m = B_x^2/8\pi \propto \Delta z^{-2}$ ) in the numerical results. From this figure, we see that in models 3 and 4 the magnetic pressure is still larger than the coronal gas



pressure at  $z = Z_{max}$ . This is the reason why the rise motion of the loop is not strongly decelerated in the corona in models 3 (Fig. 10c) and 4 (Fig. 10b). On the other hand, the magnetic pressure becomes equal to the coronal gas pressure at  $z < Z_{max}$  in model 5, which explains the strong deceleration of the loop expansion in the corona in this model (Fig. 10a).

---

Figure 11

---

#### iv) Effect of Initial Magnetic Field Strength : Models 6 and 7

In order to see the effect of the initial magnetic field strength, i.e.  $\beta_*$  (= the ratio of gas to magnetic pressures at the center of the initial magnetic flux sheet), we calculate the cases of  $\beta_* = 2.0$  (model 6) and  $0.5$  (model 7); other parameters are the same as in model 3 ( $\beta_* = 1$ ). The overall evolution of the system in both models is very similar to that of model 3, and the self-similar type of evolution characterized by equations (13) and (14) is again observed. It is found that the values of  $a_1$  and  $a_2$  for models 6 and 7 are different from those of model 3;  $a_1 = 0.053, a_2 = 0.23$  for model 6 ( $\beta_* = 2.0$ ) and  $a_1 = 0.070, a_2 = 0.39$  for model 7 ( $\beta_* = 0.5$ ). Thus,  $a_1$  and  $a_2$  decrease with  $\beta_*$  while the Alfvén Mach number  $a_1/a_2$  increases with  $\beta_*$  (Table 1). We also find that the values of  $a_1$  are approximately equal to  $1/2 - 1/3$  times the growth rate of the linear instability; the dependence of  $a_1$  on  $\beta_*$

Table 1

can be therefore understood on the basis of the linear instability (Table 2 in Appendix A). A more detailed nonlinear analysis shows that  $a_1$  may be determined by the free fall motion of gas along the curved magnetic loop, and is of the order of the inverse of the gas element free fall time. This is also consistent with the fact that the linear growth time is of the order of the free fall time.

#### IV. Quasi-1D Self-Similar Solutions

The most significant characteristics we observed in the present nonlinear evolution of the Parker instability is the apparent emergence of a self-similar pattern of the fluid velocity and the fields in the case of  $\lambda < X_{max}$ . As mentioned in §IIIb, the vertical distributions of  $V_z$  (vertical component of fluid velocity) and  $V_A$  (local Alfvén speed) at the middle of the magnetic loop show self-similar behavior, as shown in Figures 5, 7 and 10. We shall now look for a self-similar solution of the problem by analytical methods, and try to shed more light on the physics of the rising motion of the magnetic loop.

Numerical results show that both  $V_z$  and  $V_A$  increase in proportion to the loop height, and that their gradient  $a_1$  and  $a_2$  are independent of time,

$$V_z = a_1 \Delta z, \quad (18)$$

$$V_A = a_2 \Delta z, \quad (19)$$

where

$$\Delta z = z - z_0,$$

and  $z_0$  is the initial height of the magnetic loop. We have the following relation from equation (18),

$$\frac{\partial V_z}{\partial \tau} = \frac{\partial V_z}{\partial t} + V_z \frac{\partial V_z}{\partial z} = a_1 V_z, \quad (20)$$

where  $\tau$  is the time in Lagrangian coordinates, while  $t$  and  $z$  are the Eulerian coordinates. Equation (20) leads to

$$V_z \propto \exp(a_1 \tau) \quad (21)$$

on a Lagrangian spatial grid. In other words, the rise velocity of each magnetic loop increases exponentially with time. In Appendix B, we examine more general self-similar solutions. Our observation clearly shows that the realized solution corresponds to the case of  $Z\ddot{Z}/\dot{Z} = 1$  in Table 3. By combining equation (18) with equation (21), we obtain an analytical expression for the vertical distribution of  $V_z$  as a function of Lagrangian coordinates  $\xi$  and  $\tau$ ,

$$V_z(\xi, \tau) = a_1 \xi \exp(a_1 \tau), \quad (22)$$

where

$$\xi = (z - z_0) - \int V_z(\xi, \tau) d\tau. \quad (23)$$

Thus, the relation between Euler variables  $(z, t)$  and Lagrangian variables  $(\xi, \tau)$  becomes

$$\xi = (z - z_0) \exp(-a_1 \tau), \quad (24)$$

$$\tau = t. \quad (25)$$

We now assume the problem is quasi-one-dimensional (quasi-1D), i.e., we consider only vertical ( $z$ ) variations of the physical quantities at the middle point of the loop. The basic equations for our quasi-1D problem are

$$\frac{\partial \rho}{\partial t} = -\frac{\partial}{\partial z}(\rho V_z) - \frac{\partial}{\partial x}(\rho V_x), \quad (26)$$

$$\frac{\partial V_z}{\partial t} + V_z \frac{\partial V_z}{\partial z} = -\frac{1}{\rho} \left[ \frac{\partial}{\partial z} \left( \frac{B_x^2}{8\pi} \right) + \frac{B_x^2}{4\pi R} \right], \quad (27)$$

$$\frac{\partial B_x}{\partial t} = -\frac{\partial}{\partial z} (B_x V_z), \quad (28)$$

where  $R$  is the radius of curvature of field lines at the middle point of the magnetic loop. The last term on the right hand side of equation (27) is in a simplified phenomenological form in order to keep the variation in one ( $z$ ) direction (the “quasi” one dimension); a similar treatment may be found in Brunel and Tajima (1983). Here we neglect the gas pressure gradient and the gravitational forces in equation (27), and  $B_z$ -related terms in equation (28). The neglect of  $B_z$ -related terms may be justified because  $B_z \ll B_x$  near the middle point of the magnetic loop; and the reason why the gas pressure gradient and the gravitational forces are neglected will become clear after the self-similar solutions are found.

A central Ansatz of the present quasi-one-dimensional model is

$$\frac{\partial}{\partial x} (\rho V_x) = (N - 1) \frac{\partial}{\partial z} (\rho V_z). \quad (29)$$

We further write

$$R = c\Delta z, \quad (30)$$

where  $N$  and  $c$  are the parameters which should be determined from the 2-D dynamics of the problem, and generally depend on time and space. However,  $N$  and  $c$  are assumed here to be constants. The left hand term in equation (29) corresponds to fluid leaking away from the midsection of the loop because the bent loop allows the fluid to escape along the field line under the

gravitational influence. In the present quasi-one-dimensional model, we measure the amount of matter leakage in the horizontal direction in terms of the vertical flow motion. This Ansatz equation (29) appears reasonable because in steady state ( $N = 0$ ), equation (29) reduces to the usual steady state continuity equation (eq. [26]); if  $N = 1$ , no leakage arises, which corresponds to a pure one dimensional motion (see Apeendix E). In order to have matter leakage,  $N < 1$ .  $N - 1$  is a parameter that measures severity of matter leakage in the  $x$ -direction. Equation (30) is a manifestation of the self-similar evolution of the spatial pattern of the loop.

Since it is convenient to use Lagrangian coordinates  $(\xi, \tau)$ , the quasi-1D equations are rewritten by using the relations between the Euler derivatives and Lagrangian derivatives,

$$\frac{\partial}{\partial z} = \exp(-a_1 \tau) \frac{\partial}{\partial \xi}, \quad (31)$$

$$\frac{\partial}{\partial t} = -a_1 \xi \frac{\partial}{\partial \xi} + \frac{\partial}{\partial \tau}. \quad (32)$$

We then have equations described by Lagrangian coordinates,

$$\frac{\partial \rho}{\partial \tau} = -(N - 1) \frac{V_z}{f} \frac{\partial \rho}{\partial \xi} - N \frac{\rho}{f} \frac{\partial V_z}{\partial \xi}, \quad (33)$$

$$\frac{\partial V_z}{\partial \tau} = -\frac{1}{\rho f} \left[ \frac{\partial}{\partial \xi} \left( \frac{B_x^2}{8\pi} \right) + \frac{B_x^2}{4\pi c \xi} \right], \quad (34)$$

$$\frac{\partial B_x}{\partial \tau} = -\frac{B_x}{f} \frac{\partial V_z}{\partial \xi}, \quad (35)$$

where

$$f = \exp(a_1 \tau). \quad (36)$$

When we insert equation (22) into equation (35), we obtain

$$\partial B_x / \partial \tau = -B_x a_1. \quad (37)$$

Thus,  $B_x$  has the following functional form,

$$B_x(\xi, \tau) = b(\xi) \exp(-a_1 \tau). \quad (38)$$

Similarly, from dimensional arguments (or from equation 14), we have

$$\rho(\xi, \tau) = r(\xi) \exp(-4a_1 \tau). \quad (39)$$

The unknown functions  $b(\xi)$  and  $r(\xi)$  are determined from equations (33) and (34). By inserting equations (22), (38) and (39) into equations (33) and (34), it follows that

$$-4r = -(N-1)\xi \frac{dr}{d\xi} - Nr, \quad (40)$$

and

$$a_1^2 \xi = -\frac{b}{4\pi r} \left( \frac{db}{d\xi} + \frac{b}{c\xi} \right). \quad (41)$$

If  $N \neq 1$ , equations (40) and (41) have the solutions

$$r(\xi) = r_1 \xi^{-(4-N)/(1-N)}, \quad (42)$$

$$b(\xi) = b_1 \xi^{-(2+N)/2(1-N)}, \quad (43)$$

where

$$r_1 = r(\xi = 1),$$

$$b_1 = a_1 \left[ \frac{8\pi r_1}{\left( \frac{2+N}{1-N} \right) - \frac{2}{c}} \right]^{1/2}.$$

Summarizing the results, we have the final solution for the quasi-1D self-similar evolution of a rising magnetic flux tube:

$$V_z = a_1 \xi \exp(a_1 \tau) = a_1 \Delta z, \quad (44)$$

$$\rho = r_1 \xi^{\frac{-(4-N)}{(1-N)}} \exp(-4a_1 \tau) = r_1 \Delta z^{\frac{-(4-N)}{(1-N)}} \exp\left[\frac{3N}{(1-N)} a_1 t\right], \quad (45)$$

$$B_x = b_1 \xi^{\frac{-(2+N)}{2(1-N)}} \exp(-a_1 \tau) = b_1 \Delta z^{\frac{-(2+N)}{2(1-N)}} \exp\left[\frac{3N}{2(1-N)} a_1 t\right], \quad (46)$$

where  $N \neq 1$  and  $\Delta z = z - z_0$ . From these solutions, the Alfvén speed becomes

$$V_A = V_{A1} \xi \exp(a_1 \tau) = V_{A1} \Delta z, \quad (47)$$

where

$$V_{A1} = b_1 / (4\pi r_1)^{1/2} = a_1 \left[ \frac{2}{\left(\frac{2+N}{1-N}\right) - \frac{2}{c}} \right]^{1/2}. \quad (48)$$

Note that the Alfvén speed, as well as the flow velocity, grow exponentially in time on each magnetic loop, i.e. on a Lagrangian coordinate ( $\xi = \text{const.}$ ), because of the ever diluting atmosphere due to matter leakage by the loop deformation. Figures 12, 13 and 14 illustrate the time evolution of  $V_z$ ,  $\rho$ , and  $B_x$  in this self-similar solution for  $N = 0$  (Fig. 13) and  $-0.5$  (Fig. 14).

---

Figure 12

Figure 13

Figure 14

---



Since  $V_{A1}$  is equal to  $a_2$  in our numerical results, we can empirically determine the value of  $N$  by equating the theoretical expression for  $V_z/V_A = a_1/a_2 = a_1/V_{A1}$  to the empirical value  $a_1/a_2 \simeq 0.2 \equiv \epsilon$  for the case shown in §IIIb)-ii). Consequently, we have

$$N = \frac{2\epsilon^2 - 2(1 - \frac{1}{c})}{2\epsilon^2 + 1 + \frac{2}{c}}. \quad (49)$$

If  $c \simeq 1$  in the nonlinear stage and  $\epsilon^2 \simeq 0.04 \ll 1$ , we find  $N \simeq 0$ . The analytical solution with  $N = 0$  ( $\rho \propto \Delta z^{-4}$ ,  $B_x \propto \Delta z^{-1}$ ) agrees well with numerical solutions as shown in Figures 7c and 7d. It should be noted that the solution with  $N = 0$  corresponds to the steady state solution in Eulerian coordinates.

Let us now consider the validity of the assumption that the gas pressure gradient force and the gravitational force may be neglected. From our self-similar solution, the ratio of gravitational force to magnetic force is estimated to be

$$\frac{\rho g}{\partial/\partial z(B_x^2/8\pi)} \propto \Delta z^{-1}, \quad (50)$$

and the ratio of the gas pressure gradient force to the magnetic force is

$$\frac{\partial p/\partial z}{\partial/\partial z(B_x^2/8\pi)} \simeq (C_s/V_A)^2 \propto \Delta z^{-2}. \quad (51)$$

Hence, as the magnetic loop rises (i.e., as  $\Delta z$  increases), the gravitational force and the gas pressure gradient force decrease more rapidly than the magnetic force. If the force ratio is evaluated on the Lagrangian spatial coordinate  $\xi = \Delta z \exp(-a_1 t) = \text{const.}$ , then the above force ratios decrease

exponentially with time. Consequently, we confirm a posteriori that as long as both force ratios are less than unity at  $t = 0$ , the neglect of the gravitational and the gas pressure gradient forces is valid.

(It should be noted that it is the gravitational force which drives the sliding motion of gas along magnetic loops. Since the evacuation of loops by this sliding motion is the cause of expansion of magnetic loops, the gravitational force is the ultimate cause of our magnetic loop expansion, even if the gravitational force can be neglected in the analysis discussed above. In fact, the growth rate of the linear instability as well as the coefficient  $a_1$  is a function of the gravitational acceleration according to more detailed nonlinear analysis.)

We briefly comment on the question why  $V_z$  increases in proportion to the height. More general analyses (Appendix B) show that the solution with  $V_z \propto \Delta z^\delta$  ( $\delta \neq 1$ ) diverges at a point with finite  $\Delta z$ , except for the case of  $N = 0$ . Although our numerical solutions show  $N \simeq 0$ ,  $N$  may not be exactly equal to 0. Thus, the solution with  $\delta = 1$  appears in the numerical results, and simulations show that such a solution is stable and proves to be an attractor. (When the numerical results correspond to the solutions deviated from the ideal self-similarity, the above argument may not necessarily hold.)

Appendix B also shows that there is another class of similarity solutions with power-law time dependence, in addition to our solution with exponential time dependence. Although such power-law solutions cannot be applied to the rising motion of magnetic loops in the chromosphere, it may be applicable

to the later phase of the rising motion of loop, i.e., after the loop enters the corona. For example, Figure 10b (model 4) shows approximately  $V_z \propto \Delta z/t$  between  $t = 45.6$  and  $56.4$ , which agrees with the power law solution in the case of  $Z\ddot{Z}/\dot{Z} \neq 1, \delta = 1, N \neq 1$  in Table 3.

## V. Summary and Discussions

### a) Summary of Numerical and Analytical Results

In this paper, we have reported results of simulations of the nonlinear evolution of the Parker instability occurring in an isolated magnetic flux sheet imbedded in a two-temperature-layered atmosphere under constant gravitational acceleration. Such an atmosphere may be a highly simplified model of solar and stellar corona-chromosphere/photosphere systems, and may be also applied to corona (halo)-disk systems in galaxies and in accretion disks.

The most important results are for the nonlinear kinematics of the rising magnetic loops. These are summarized as follows:

(1) In the nonlinear regime, the rise velocity ( $V_z$ ) of the magnetic loop and the local Alfvén speed ( $V_A$ ) at the top of the rising magnetic loop increases with height as long as the loop is in the low temperature atmosphere. When the horizontal size ( $X_{max}$ ) of the computing domain is fixed to the wavelength ( $\lambda$ ) of the initial perturbation, the expansion of the magnetic loop is not self-similar, and the magnetic field is nearly current free with  $B_x \propto \exp(-\Delta z/H_m)$ , where  $\Delta z$  is the height from the base of the initial magnetic flux sheet, and  $H_m \simeq 6.4H \simeq (\lambda/\pi)H$ . On the other hand, when  $X_{max} \gg \lambda$ , the expansion of the magnetic loop shows self-similar evolution with height:  $B_x \propto \Delta z^{-1}$ ,  $\rho \propto \Delta z^{-4}$ ,  $V_z/C_s = a_1 \Delta z/H$ , and  $V_A/C_s = a_2 \Delta z/H$ . Thus, the local Alfvén Mach number  $V_z/V_A = a_1/a_2$

is nearly constant with height. Both  $a_1 (= 0.05 - 0.07)$  and  $a_2 (= 0.2 - 0.4)$  decrease with  $\beta_*$ , while  $a_1/a_2 (= 0.18 - 0.23)$  increase with  $\beta_*$ , for  $0.5 \leq \beta_* \leq 2.0$ . The values of  $a_1$  are approximately equal to  $1/2 - 1/3$  times the growth rates of the linear instability.

(2) After the loop enters the corona, the acceleration of the rising motion of the loop decreases, and the motion eventually decelerates. The deceleration is not as strong if the effective horizontal wavelength increases as the loop rises (models 2 and 3). When the height of the coronal base ( $Z_{cor}$ ) is larger (smaller), the maximum rise velocity of the loop is larger (smaller) (models 4 and 5).

(3) A quasi one-dimensional self-similar solution is found analytically, which describes the vertical variation of physical quantities at the center of a rising magnetic loop in the case of  $\lambda \ll X_{max}$ . The solution has the characteristics that in Eulerian coordinates  $V_z \propto \Delta z$  and  $V_A \propto \Delta z$  are stationary, and  $\rho \propto \Delta z^{\frac{-(4-N)}{1-N}}$  and  $B_x \propto \Delta z^{\frac{-(2+N)}{2(1-N)}}$  have exponential time dependence (including the special case of steady state [ $N = 0$ ] where  $N$  is the parameter defining the strength of downflow along the loop [note that  $N = 1$  corresponds to the case of no downflow.]) Our numerical simulations show  $N \simeq 0$ . From these results, we find that the rising velocity ( $V_z$ ) and  $V_A$  of each magnetic loop (i.e., in Lagrangian coordinates) increases exponentially with time, while  $\rho$  and  $B_x$  decrease exponentially with time.

Let us now discuss qualitatively the physical reasons for the above results.

First, the reason why the rise velocity of the loop increases with height is the steep pressure (density) gradient of the background atmosphere. That is, when the magnetic flux rises to a new position which is at a finite distance from the original position, the new state is still Parker-unstable, e.g., magnetic buoyancy is larger than the restoring magnetic curvature force. (Infinitesimal displacements correspond to the linear instability.) Thus, the continuing acceleration occurs as long as the loop is in the lower temperature atmosphere. If the magnetic loop enters the Parker-stable region, such as the corona (when the larger scale height is due to high temperature; this paper) or small gravity region (when the larger scale height is due to small  $g$ ; Matsumoto et al. 1988), the magnetic loop is decelerated. However, if the effective wavelength of the magnetic loop can become larger than the critical wavelength of the Parker instability in the new state by e.g. lateral expansion of the magnetic loop as shown in models 2 and 3, then continuing acceleration will be realized.

The self-similar solution reveals that in the fully nonlinear stage of the magnetic loop expansion in the low temperature atmosphere, the magnetic force dominates the gravitational and the gas pressure gradient forces. Thus, the word ‘magnetic buoyancy’ is not strictly suitable to describe the dynamics in the fully nonlinear stage; we should say that the magnetic loop is accelerated by the magnetic pressure gradient force. In this sense, the process is similar to the 1D free expansion of magnetized cold gas into vacuum.

It should be, however, noted that the expansion velocity of the 1D free expansion of magnetized gas is constant, while expansion speed increases with height in our case; this is because there is a downflow along the magnetic loop in our models: The downflow evacuates the loop and increases the local Alfven speed. This latter effect is another reason why the expansion velocity increases with height. We can also understand the deceleration of the magnetic loop after it enters the corona from these points of view: Since the scale height is large in the corona, the pressure does not steeply decrease; hence the expansion of the magnetic loop is not 'free' in the corona, i.e. loop suffers deceleration by the gas pressure force.

#### b) Application to Emerging Magnetic Flux in the Solar Atmosphere

There are suggestions in available data that the calculations reported here may be relevant to solar magnetic flux emergence (Suematsu 1987, Chou 1988). Consider, for example, the AFS (Arch Filament System), which corresponds to the later phase of magnetic flux emergence. Bruzek (1967, 1969) found that the velocity of the rising loop is about 10 km/s, approximately 0.2 times of the Alfven speed in the middle chromosphere, and that the velocity of downflows along the loop is about 50 km/s, roughly equal to the local Alfven speed. These phenomena are fairly well represented by model 3 of this paper. Furthermore, if we apply our results to the emergence of magnetic flux tubes in coronal holes, we predict that the rise velocities and the

downflows in AFS filament are larger in coronal holes than in quiet regions by 10 - 20 percent, because the height of the coronal base in coronal holes is larger than in quiet regions by 2-3 (low temperature domain) scale heights (e.g. Shibata and Suematsu 1982).

Our simulation results are also consistent with the observed small rise velocity of magnetic flux tube at the photospheric level (Chou and Wang 1987); Kawaguchi and Kitai (1976) reported velocities  $\leq 0.2$  km/s, and Brants (1985) found velocities  $\simeq 1$  km/s. For example, if we assume  $C_s \simeq 10$  km/s,  $H \simeq 200$  km,  $\Delta z$  is the height from the photospheric base, and use the relation  $V_z/C_s = 0.06\Delta z/H$  in model 3, we find that  $V_z \leq 1$  km/s at  $\Delta z \leq 400$  km and  $V_z \simeq 10$  km/s at  $\Delta z \simeq 4000$  km. The former velocity and height correspond to those of photospheric emerging flux and the latter to those of AFS. We also find transient strong downdrafts at the footpoint of the magnetic loop in the numerical results of model 3:  $V_z \simeq 1-2$  km/s at  $\Delta z \simeq 200-600$  km/s in the initial stage of the magnetic loop expansion. These downdrafts may correspond to those observed by Kawaguchi and Kitai (1976) (see also Shibata 1980).

It should be noted that the actual process of magnetic flux emergence in the solar atmosphere is a three dimensional process. Thus, the interchange mode ( $k_y \neq 0$ ) will couple to the undular mode, and the processes may be different from those (for  $k_y = 0$ ) studied in the present paper. Although we think that the interchange mode is essential for the creation of isolated flux



tube from the sheet, the essence of the dynamics of the flux emergence is not so different from that found in this paper. This is because for finite turbulent viscosity, we assume that the growth rate for  $k_{y,cut}$  is comparable to that for  $k_y = 0$  (Schmitt and Rosner 1982).

The dynamics studied in the present paper may also be related to the energy storage process in the solar flares. Steinolfson and Tajima (1987) examined the nonlinear twisting process of magnetic flux tube by the photospheric footpoint motion; and Bekki *et al.* (1988) studied the nonlinear evolution of force free field associated with the shear motion of footpoints. In these studies, the footpoint motions are assumed to be given as the boundary condition. However, it is possible that these photospheric motion may be a result of the emergence of a twisted magnetic flux tube (Tanaka 1987, Kurokawa 1988). In order to discuss the relation of flux emergence with flares, a more detailed study including 3-D processes will have to be made.

### c) Application to Other Astrophysical Loop-like Phenomena

Finally, we comment on the application of our results to loop-like mass ejection from astrophysical objects. It is well known that coronal transients often show a loop-like (or bubble-like) configuration (Wagner 1984, Sime *et al.* 1984). In some transients, downflow-like features are observed along the legs of the transients in the inner corona ( $R \leq 1.6R_\odot$ ). These characteristics are consistent with those seen in our simulation results. Thus, the essential

This work was also supported in part by the US-Japan Cooperative Science Program "Simulation Studies of Cosmical Magnetodynamical Phenomena (Rosner-Uchida)".

## Appendix A

### Characteristics of Linear Instability of Isolated Magnetic Flux Sheet

We here summarize the main characteristics of the linear instability of an isolated magnetic flux sheet considered in the present paper.

We have performed a linear stability analysis using the normal mode method similar to those of Horiuchi *et al.* (1988) and Matsumoto and Horiuchi (1988). That is, we first linearize the basic equations (1)–(6) by assuming  $B_x = B_0 + b_x$ ,  $|b_x/B_0| \ll 1$ , and  $b_x = \tilde{b}_x \exp(i\omega t + ik_x x + ik_y y)$ , etc. After some manipulations, the linearized equations become

$$\frac{d}{dz} \begin{bmatrix} \xi \\ \eta \end{bmatrix} = \begin{bmatrix} D_{\xi\xi} & D_{\xi\eta} \\ D_{\eta\xi} & D_{\eta\eta} \end{bmatrix} \begin{bmatrix} \xi \\ \eta \end{bmatrix}, \quad (\text{A1})$$

where

$$D_{\xi\xi} = \frac{1}{1+\beta} \frac{d \ln \beta}{dz} - \frac{d \ln T}{dz} - \frac{g}{C_s^2} \frac{\beta\gamma}{1+\beta} \frac{(1+\beta\gamma-\beta)\omega^2 - 2k_x^2 C_s^2}{(2+\beta\gamma)\omega^2 - 2k_x^2 C_s^2}, \quad (\text{A2})$$

$$D_{\xi\eta} = -\frac{\beta\gamma}{C_s^2} \frac{\beta\gamma\omega^4 - \omega^2(2+\beta\gamma)k_x^2 C_s^2 + 2k_x^2 k_y^2 C_s^4}{[(2+\beta\gamma)\omega^2 - 2k_x^2 C_s^2][\beta\gamma\omega^2 - 2k_x^2 C_s^2]}, \quad (\text{A3})$$

$$D_{\eta\xi} = \omega^2 - \frac{2}{\beta\gamma} k_x^2 C_s^2 + g \left( \frac{1}{1+\beta} \frac{d \ln \beta}{dz} - \frac{d \ln T}{dz} \right) - \frac{1}{1+\beta} \frac{g^2 \beta\gamma(1+\beta\gamma-\beta)\omega^2 + 2(1+\beta-\beta\gamma)k_x^2 C_s^2}{C_s^2 [(2+\beta\gamma)\omega^2 - 2k_x^2 C_s^2]}, \quad (\text{A4})$$

$$D_m = -\frac{g}{C_s^2} \frac{\beta\gamma\omega^2}{(2 + \beta\gamma)\omega^2 - 2k_x^2 C_s^2}, \quad (\text{A5})$$

and

$$\begin{aligned} \xi &= \rho_0 \tilde{v}_z, \\ \eta &= i\omega(\delta\tilde{p} + \frac{B_0 \tilde{b}_x}{4\pi}), \\ k^2 &= k_x^2 + k_y^2, \end{aligned}$$

and  $\rho_0$  and  $B_0$  are the quantities in the unperturbed state, and  $\tilde{v}_z, \delta\tilde{p}, \tilde{b}_x$  are perturbed quantities. Here, we used the equation (9) of magnetostatic balance for the unperturbed quantities, and  $\beta = \beta(z)$  and  $T = T(z)$  are given in equations (7) and (8) in the text. If we assume  $d\ln\beta/dz = 0$  and  $d\ln T/dz = 0$ , the equations (A1)–(A5) are the same as those in Horiuchi *et al.* (1988), and if we assume only  $d\ln\beta/dz = 0$ , the equations are the same as those of Matsumoto and Horiuchi (1988).

The boundary conditions are  $\xi = 0$  and  $d\eta/dz = 0$  on  $z = 0$ , and  $\xi$  and  $\eta$  should vanish at  $z \rightarrow \infty$ . The equations (A1)–(A5) are solved numerically for prescribed  $k_x$  and  $k_y$  using the Runge-Kutta method to find an eigenvalue  $\omega$  and the corresponding eigenfunctions which satisfy these boundary conditions.

---

Figure A1

---

Figure A1 shows the growth rates  $i\omega$  as a function of the horizontal wavenumber  $k_x$  for three cases  $\beta_* = 0.5, 1.0$ , and  $2.0$  for  $k_y = 0$ , and Table 2 shows the growth rate as a function of  $\beta_*$  for  $k_x = 0.314$  ( $\lambda = 20$ ) and  $k_y = 0$ . Note that the horizontal wavelength ( $\lambda = 20$ ) considered in the present paper is close to the wavelengths for the maximum growth rates for  $\beta_* = 0.5, 1.0$ , and  $2.0$ . From Table 2, we see that the growth rates tend to a non-zero value when  $\beta_*$  becomes 0 for  $D = 4$  and  $8$  in the case of  $T_{cor}/T_{ch} = 25$ , and for all finite  $D$ 's in the case of  $T_{cor}/T_{ch} = 1$ . This behavior is quite different from that for the case of a non-isolated field (Parker 1966, Horiuchi *et al.* 1988, Matsumoto and Horiuchi 1988), where the growth rates tend to zero when  $\beta_*$  becomes 0. This is because in the case of isolated field the density is locally larger just above the flux sheet than in the sheet, i.e., the density inversion occurs locally as in the case of a familiar magnetic Rayleigh-Taylor instability (Kruskal and Schwarzschild 1954, Parker 1979, Priest 1981). When the magnetic field is confined in the half space  $z < 0$  with a sharp boundary at  $z = 0$  by the heavy material in  $z > 0$ , and when the plasma  $\beta$  tends to 0 in the lower layer, the growth rate tends to a non-zero value  $\sqrt{gk_x - 2k_x^2 C_s^2}$  for  $k_y = 0$  and  $\gamma = 1$ , where  $C_s$  is the sound speed in the upper layer (Parker 1979, Priest 1981).

Table 2

---

Figure A2

---

Figure A2 shows the 1-D eigenfunctions (as a function of  $z$ ) for some physical quantities. It is noted that both velocities  $\bar{v}_x$  and  $\bar{v}_z$  are maximum at the height near the top of the flux sheet ( $z \simeq 8$ ), and that they have non-negligible values even above the flux sheet. The same is true for the magnetic field, density and gas pressure.

## Appendix B

### General Self-Similar Solutions of Quasi-1D MHD Equations in the case of $\lambda \ll X_{max}$

In this Appendix, we shall show that there is another class of self-similar solutions with power-law time dependence, in addition to the empirical solution with exponential time dependence discussed in §IV.

As in Zeldovich and Raizer (1967), we seek a general self-similar solution by adopting the new dimensionless independent variable

$$\zeta = \frac{\Delta z}{Z(t)}, \quad (B1)$$

$$\tau = \frac{t}{t_0}, \quad (B2)$$

where  $Z(t)$  is the scale function, with dimension of length, and  $t_0$  is a normalization constant for the time. We further assume

$$V_z = \dot{Z}(\tau)v(\zeta)/t_0, \quad (B3)$$

$$\rho = \Sigma(\tau)\sigma(\zeta), \quad (B4)$$

$$B_x = (4\pi\Sigma\dot{Z}^2)^{1/2}b(\zeta)/t_0, \quad (B5)$$

where  $v$ ,  $\sigma$ , and  $b$  are nondimensional quantities with only  $\zeta$ -dependence, and the dot represents  $d/d\tau$ . Substituting equations (B1)–(B5) into equations (26)–(30), we have

$$\frac{\dot{\Sigma}}{\Sigma} \frac{Z}{\dot{Z}} + Nv' + (Nv - \zeta) \frac{\sigma'}{\sigma} = 0, \quad (B6)$$

$$\frac{Z\ddot{Z}}{\dot{Z}^2} v + (v - \zeta)v' + \frac{b^2}{\sigma} \left( \frac{b'}{b} + \frac{1}{c\zeta} \right) = 0, \quad (B7)$$

$$\frac{Z\ddot{Z}}{\dot{Z}^2} + \frac{1}{2} \frac{\dot{\Sigma}}{\Sigma} \frac{Z}{\dot{Z}} + (v - \zeta) \frac{b'}{b} + v' = 0, \quad (B8)$$

where  $' \equiv d/d\zeta$ .

We adopt the boundary condition for  $v(\zeta)$

$$v(\zeta = 0) = 0 \quad (B9)$$

because there is no magnetic flux below  $\zeta = 0$ , and thus the fluid is stationary there. Thus,  $v(\zeta)$  may be written as a self-similar function that satisfies equation (B9),

$$v(\zeta) = \zeta^\delta, \quad (B10)$$

where  $\delta$  is a positive real number. Several solutions satisfying equations (B6)–(B8) and equation (B10) are summarized in Table 3 for both  $Z\ddot{Z}/\dot{Z}^2 = 1$  and  $\neq 1$ .

Table 3



Table 1

Models examined in this paper ( $\gamma = 1.05$ ,  $D = 4$ ,  $T_{cor}/T_{ch} = 25$ ) and results of nonlinear simulations

model name	$\lambda$	$X_{max}$	$\beta_*$	$Z_{cor}$	$V_{z,max}$	$a_1$	$a_2$	$a_1/a_2$
model 1	20	20	1	18	1.25			
model 2	20	40	1	18	1.4			
model 3	20	80	1	18	1.4	0.062	0.30	0.21
model 4	20	80	1	15	1.1			
model 5	20	80	1	12	0.45			
model 6	20	80	2.0	18	—	0.053	0.23	0.23
model 7	20	80	0.5	18	—	0.070	0.39	0.18

Note:  $\lambda$  is the wavelength of the initial perturbation,  $X_{max}$  is the horizontal size of the computing domain,  $\beta_*$  is the plasma  $\beta_*$  (= gas pressure/magnetic pressure) defined at the center of the initial magnetic flux sheet,  $Z_{cor}$  is the initial height of the coronal base,  $V_{z,max}$  is the maximum velocity at  $x = X_{max}/2$ ,  $a_1$  and  $a_2$  are defined by  $a_1 = V_z/\Delta z$  and  $a_2 = V_A/\Delta z$ , where  $V_z$  is the rise velocity of the magnetic loop, and  $V_A$  is the local Alfvén speed at  $x = X_{max}/2$ . The units of the length and the velocity are  $H$  and  $C_s$ .

Table 2

Dependence of Linear Growth Rates on  $\beta_*$ ,  $D(=z_1 - z_0)$ , and  $T_{cor}/T_{ch}$ ,

when  $k_x = 0.314$ ,  $k_y = 0$ ,  $\gamma = 1.05$ ,  $Z_{max} = 35$ ,  $Z_{cor} = 18$ ,  $w_{tr} = 0.6$  and

$$w_0 = w_1 = 0.5.$$

$\beta_*$	4.0	2.0	1.0	0.5	0.333	0.1	0.01	0.001
$T_{cor}/T_{ch} = 25$								
D=4	0.008	0.080	0.121	0.150	0.162	0.181	0.190	0.192
D=8	0.047	0.104	0.144	0.169	0.177	0.189	0.192	0.191
D=12	0.041	0.097	0.120	0.100	0.049	stable		
D=16	0.033	0.087	0.097	stable				
$T_{cor}/T_{ch} = 1$								
D=4	0.008	0.080	0.121	0.150	0.162	0.181	0.190	0.192
D=8	0.047	0.104	0.144	0.169	0.178	0.189	0.193	0.194
D=16	0.063	0.119	0.155	0.175	0.181	0.190	0.194	0.194
Parker	stable	stable	0.158	0.191	0.188	0.137	0.049	0.012

The unit of the growth rate is  $C_s/H$ . The growth rates obtained by equation (13.34) of Parker (1979) are also shown.

Table 3

## Summary of Self-Similar Solutions

$Z\ddot{Z}/\dot{Z}^2$	$\delta$	$N$	characteristics of solutions
$Z\ddot{Z}/\dot{Z}^2 \neq 1$  [ $Z \propto \tau^\alpha$ ]	$\delta \neq 1$	$N \neq 0$	no solution
		$N = 0$	steady solution in Eulerian coordinates $\alpha = 1/(1 - \delta)$ $\delta < 1 : V_z \propto \tau^{\delta/(1-\delta)} \zeta^\delta \propto \Delta z^\delta$ $B_x \propto \tau^{-\delta/(1-\delta)} \zeta^{-\delta} \propto \Delta z^{-\delta}$ $\delta > 1 : V_z \propto (\tau_c - \tau)^{-\delta/(\delta-1)} \zeta^\delta \propto \Delta z^\delta$ $B_x \propto (\tau_c - \tau)^{\delta/(\delta-1)} \zeta^{-\delta} \propto \Delta z^{-\delta}$ (note that $Z \propto (\tau_c - \tau)^\alpha$ when $\delta > 1$ )
	$\delta = 1$	$N \neq 1$	nonsteady solution with power law time dependence $V_z \propto \tau^{\alpha-1} \zeta \propto \Delta z/t$ $B_x \propto \tau^{-\alpha} \zeta^Y \propto t^{-(Y+1)\alpha} \Delta z^Y$ where $Y = [2 - N + (2 - 4\alpha)/\alpha]/[2(1 - N)]$
		$N = 1$	nonsteady solution with power law time dependence $\alpha = 2/3$ $V_z \propto \tau^{-\frac{1}{3}} \zeta \propto \Delta z/t$ $B_x \propto \tau^{-\frac{2}{3}} \zeta^{\frac{1}{2} - \frac{1}{\epsilon}} \propto t^{-1 + \frac{2}{3\epsilon}} \Delta z^{\frac{1}{2} - \frac{1}{\epsilon}}$
	$\delta \neq 1$	any $N$	no solution
$Z\ddot{Z}/\dot{Z}^2 = 1$  [ $Z \propto \exp(a\tau)$ ]	$\delta = 1$	$N \neq 1$	solution with exponential time dependence $V_z \propto \zeta \exp(a\tau) \propto \Delta z$ $B_x \propto \zeta^{\frac{-(2+N)}{2(1-N)}} \exp(-a\tau) \propto \Delta z^{\frac{-(2+N)}{2(1-N)}} \exp[\frac{3N}{2(1-N)} \frac{a}{t_0} t]$
		$N = 1$	no solution

Note:  $\zeta = \Delta z/Z(\tau)$  and  $\tau = t/t_0$  are Lagrangian coordinates, and  $\Delta z$  and  $t$  are Eulerian coordinates, where  $\Delta z = z - z_0$  is the height measured from the base of the initial magnetic flux tube, and  $Z = Z(t)$  is the scale function defined in equation (B1).  $B_x$  is the strength of horizontal component of magnetic field at the midpoint of the expanding magnetic loop.  $\delta$  is the exponent of velocity function ( $V_z \propto \Delta z^\delta$ ) defined in equation (B10),  $N$  is the parameter defining the strength of the downflow along the magnetic loop (eq. [29]) in §IV], and  $c = R/\Delta z$ , where  $R$  is the radius of curvature of magnetic loop (eq. [30]).

## REFERENCES

- Acheson, D. J. 1979, *Solar Phys.*, **62**, 23.
- Asseo, E., Cesarsky, C. J., Lachieze-Rey, M. and Pellat, R. 1978, *Ap. J. (Letters)*, **225**, L21.
- Asseo, E. and Sol, H., 1987, *Phys. Reports*, **148**, 307.
- Bateman, G. 1978, *MHD Instabilities* (Cambridge: MIT Press).
- Baierlein, R., Schwing, E., and Herbst, W. 1981, *Icarus*, **48**, 49.
- Bekki, N., Tajima, T., Mikic, Z., Barnes, D. C., Schnack, D. D. 1988, *Phys. Rev. Lett.*, in press.
- Brants, J. J. 1985, *Solar Phys.*, **98**, 197.
- Brunel, F. and Tajima, T. 1983, *Phys. Fluid*, **26**, 535.
- Brunel, F., Leboeuf, J. N., Tajima, T., and Dawson, J. M. 1981, *J. Comp. Phys.*, **43**, 268.
- Bruzek, A. 1967, *Solar Phys.*, **2**, 451.
- Bruzek, A. 1969, *Solar Phys.*, **8**, 29.
- Byrne, P. B. and Rodono, M. (ed.) 1983, in *IAU Colloq. No. 71*, *Activity in Red Dwarf Stars* (Dordrecht: Reidel).
- Chou, D. 1988, private communication.
- Chou, D. and Wang, H. 1987, *Solar Phys.*, **110**, 81.
- Duric, N., Seaquist, E. R., Crane, P. C., Bignell, R. C., and Davis, L. E. 1983, *Ap. J., Lett*, **273**, L11.
- Elmegreen, B. G. 1982, *Ap. J.*, **253**, 634.

- Fujimoto, M. and Sawa, T. 1987, *Pub. Astr. Soc. Japan*, **39**, 375.
- Galeev, A. A., Rosner, R., and Vaiana, G. S. 1979, *Ap. J.*, **229**, 318.
- Horiuchi, T., Matsumoto, R., Hanawa, T. and Shibata, K. 1988, *Pub. Astr. Soc. Japan*, **40**, 147.
- Hughes, D. W. and Cattaneo, F. 1987, *Geophys. Ap. Fluid Dyn.*, **39**, 65.
- Hughes, D. W. and Procter, M. R. E. 1988, *Ann. Rev. Fluid Mech.*, **20**, 187.
- Hummel, E., van Gorkom, J. H., and Kotanyi, C. G. 1983, *Ap. J. (Letters)*, **267**, L5.
- Kato, S. and Horiuchi, T. 1985, *Pub. Astr. Soc. Japan*, **37**, 399.
- Kato, S. and Horiuchi, T. 1986, *Pub. Astr. Soc. Japan*, **38**, 313.
- Kawaguchi, I. and Kitai, R. 1976, *Solar Phys.*, **46**, 125.
- Kruskal, M. D. and Schwarzschild, M. 1954, *Proc. Roy. Soc.*, **223A**, 348.
- Kurokawa, H. 1988, *Solar Phys.*, **113**, 259.
- Low, B. C. 1982, *Ap. J.*, **254**, 796.
- Low, B. C. 1984, *Ap. J.*, **281**, 392.
- Low, B. C., Munro, R. H. and Fisher, R. R., 1982, *Ap. J.*, **254**, 335.

- Matsumoto, R., and Horiuchi, T. 1988, *Pub. Astr. Soc. Japan*,  
to be submitted.
- Matsumoto, R., Horiuchi, T., Shibata, K. and Hanawa, T., 1988,  
*Pub. Astr. Soc. Japan*, **40**, 171.
- Moreno-Insertis, F. 1986, *Astr. Ap.*, **166**, 291.
- Mouschovias, T. CH. 1974, *Ap. J.*, **192**, 37.
- Mouschovias, T. CH., Shu, F. H., and Woodward, P. R. 1974,  
*Astr. Ap.*, **33**, 73.
- Newcomb, W. A. 1961, *Phys. Fluids*, **4**, 391.
- Ogino, T., Sanuki, H., Kamimura, T. and Takeda, S. 1981, *J. Phys.*  
*Soc. Japan*, **50**, 1698.
- Parker, E. N. 1966, *Ap. J.*, **145**, 811.
- Parker, E. N. 1969, *Space Sci. Rev.*, **9**, 651.
- Parker, E. N. 1975, *Ap. J.*, **202**, 523.
- Parker, E. N. 1979, *Cosmical Magnetic Fields* (Oxford: Clarendon Press), p. 134.
- Piddington, J. H. 1970, *M.N.R.A.S.*, **148**, 131.
- Priest, E. R. 1982, *Solar Magnetohydrodynamics* (Dordrecht: Reidel), p. 291.
- Richtmyer, R. O. and Morton, K. W. 1967, *Difference Methods for Initial Value Problems* (2nd ed., New York: Interscience), chap. 13.

- Rosner, R., Golub, L. and Vaiana, G. S., 1985, *Ann. Rev. Astr. Ap.*, **23**, 413.
- Rubin, E. and Burstein, S. Z. 1967, *J. Comp. Phys.*, **2**, 178.
- Sawa, T. and Fujimoto, M. 1986, *Pub. Astr. Soc. Japan*, **38**, 133.
- Schmitt, J. H. M. M. and Rosner, R. 1983, *Ap. J.*, **265**, 901.
- Schüssler, M. 1980, *Astr. Ap.*, **89**, 26.
- Shibata, K. 1980, *Solar Phys.*, **66**, 61.
- Shibata, K. 1983, *Pub. Astr. Soc. Japan*, **35**, 263.
- Shibata, K. and Suematsu, Y. 1982, *Solar Phys.*, **78**, 333.
- Shibata, K. and Uchida, Y. 1985, *Pub. Astr. Soc. Japan*, **37**, 31
- Shibata, K. and Uchida, Y. 1986, *Pub. Astr. Soc. Japan*, **38**, 633
- Shu, F. H. 1974, *Astr. Ap.*, **33**, 55.
- Sime, D. G., MacQueen, R. M., and Hundhausen, A. J. 1984, *J. Geophys. Res.*, **89**, 2113.
- Sofue, Y. 1973, *Pub. Astr. Soc. Japan*, **25**, 207.
- Sofue, Y., Fujimoto, M., and Wielebinsky, R. 1986, *Ann. Rev. Astr. Ap.*, **24**, 459.
- Sofue, Y. and Handa, T. 1984, *Nature*, **310**, 568.
- Spitzer, L. Jr. 1978, *Physical Processes in the Interstellar Medium* (New York: Johns and Wiley Sons).



- Spruit, H. C. and van Ballegooijen, A. A. 1982, *Astr. Ap.*, **106**, 58.
- Stella, L. and Rosner, R. 1984, *Ap. J.*, **277**, 312.
- Steinolfson, R. and Tajima, T. 1987, *Ap. J.*, **322**, 530.
- Suematsu, Y. 1987, private communication.
- Takahara, F. 1979, *Prog. Theor. Phys.*, **62**, 629.
- Tanaka, K. 1987, *Pub. Astr. Soc. Japan*, **39**, 1.
- Tosa, M. and Sofue, Y. 1974, *Astr. Ap.*, **32**, 461.
- Uchida, Y. 1986, *Ap. Space Sci.*, **118**, 127.
- Uchida, Y. and Shibata, K. 1985, *Pub. Astr. Soc. Japan*, **37**, 515.
- Uchida, Y. and Shibata, K. 1986, *Can. J. Phys.*, **64**, 507.
- Umemura, S., Iki, K., Shibata, K., and Sofue, Y. 1988, *Pub. Astr. Soc. Japan*, **40**, 25.
- Wagner, W. J. 1984, *Ann. Rev. Astr. Ap.*, **22**, 267.
- Zeldovich, Ya. B. and Raizer, Yu. P. 1967, *Physics of Shock Waves and High-Temperature Hydrodynamic Phenomena* (New York: Academic Press), vol.2.
- Zwaan, C. 1978, *Solar Phys.*, **60**, 213.
- Zwaan, C. 1987, *Ann. Rev. Astr. Ap.*, **25**, 83.
- Zweibel, G. and Kulsrud, R. M. 1975, *Ap. J.*, **201**, 63.

### Figure Captions

Fig. 1 Results for model 1, where  $\beta_* = 1$ ,  $\lambda = X_{max} = 20$ ,  $D = 4$ ,  $\gamma = 1.05$ ,  $Z_{cor} = 18$ ,  $T_{cor}/T_{ch} = 25$ . The unit of the length is  $H$ , the scale height in the lower temperature atmosphere (chromosphere). (a) the magnetic field lines  $\mathbf{B} = (B_x, B_z)$ , (b) the velocity vector  $\mathbf{V} = (V_x, V_z)$  (c) the density contours ( $\log \rho$ ). It should be noted that the size in the  $x$ -direction of these figures corresponds to twice of  $X_{max}$ . The magnetic flux between each magnetic field line is logarithmic. The scale of the velocity vector is shown below the frame of  $t=47.4$  in (b) in the unit of  $C_s$ ;  $VNM = 2.0$  indicates that the arrow with the length of this line has the velocity of  $2.0 \times C_s$ . Similarly, the scale of the length is shown also by this short line and  $XNM$  in the unit of  $H$ . Total illustrated area is  $(2X_{max} \times Z_{max}) = (40 \times 35)$ . Contour level step-width is 0.25 for (c) in the unit of logarithmic scale. Numbers in the lefthand side of each frame in (a) represent the time in units of  $H/C_s$ .

Fig. 2 The distribution in  $z$  of (a) the vertical component of velocity  $V_z$ , (b) the density ( $\log \rho$ ), (c) the local Alfvén speed ( $V_A$ ), (d) the horizontal component of magnetic field ( $\log B_x$ ), at  $x = X_{max}/2$  (middle of the rising loop) for model 1 (the case shown in Fig. 1) at  $t = 0.0, 31.6, 39.9, 45.8$ . The dashed line in (d) indicates the line of  $B_x \propto \exp(-\Delta z/H_m)$  with  $H_m = 20/\pi \simeq 6.4$ .

Fig. 3 The distributions in  $z$  of the initial gas pressure ( $p_g$ ) and the steady magnetic pressure ( $p_m$ ) for model 1 at  $x = X_{max}/2$ . Note that  $p_m =$

$B_x^2/8\pi \propto \exp[-\Delta z/(H_m/2)]$  (cf. eq.[11]) and  $H_m = 20/\pi \simeq 6.4$ , and the proportional constant is the same as that of numerical results in Figure 2d.

Fig. 4 Time variations of (a) the magnetic field lines  $\mathbf{B} = (B_x, B_z)$ , (b) the velocity vector  $\mathbf{V} = (V_x, V_z)$  (c) the density contours ( $\log \rho$ ) in model 2, where  $X_{max} = 40$  and other parameters are the same as in model 1. The total illustrated area is  $(X_{max} \times Z_{max}) = (40 \times 35)$ . Other remarks are the same as in Figure 1.

Fig. 5 The distributions in  $z$  of  $V_z$  at  $x = X_{max}/2$  (middle of the rising magnetic loop) for model 2 (the case shown in Fig. 4) at  $t = 0.0, 33.2, 40.8, 48.7, 55.1$ .

Fig. 6 Time variations of (a) the magnetic field lines  $\mathbf{B} = (B_x, B_z)$ , (b) the velocity vector  $\mathbf{V} = (V_x, V_z)$ , (c) the density contours ( $\log \rho$ ) in model 3, where  $X_{max} = 80$  and other parameters are the same as in model 1. The total illustrated area is  $(X_{max} \times Z_{max}) = (80 \times 35)$ . Other remarks are the same as in Figure 1.

Fig. 7 The distribution in  $z$  of (a) the vertical component of velocity  $V_z$ , (b) the local Alfven speed ( $V_A$ ), (c) the density ( $\log \rho$ ), (d) the horizontal component of magnetic field ( $\log B_x$ ), at  $x = X_{max}/2$  (middle of the rising loop) for model 3 (the case shown in Fig. 6) at  $t = 0.0, 33.4, 40.0, 47.0, 51.8$ . The dashed curves in (c) and (d) represents the curves of  $\rho \propto \Delta z^{-4}$  and  $B_x \propto \Delta z^{-1}$ , respectively.

Fig. 8 Time variations of (a) the magnetic field lines  $\mathbf{B} = (B_x, B_z)$ , (b) the velocity vector  $\mathbf{V} = (V_x, V_z)$ , (c) the density contours ( $\log \rho$ ) in model 4, where  $Z_{cor} = 15$  and other parameters are the same as in model 3 ( $Z_{cor} = 18$ ). The total illustrated area is  $(X_{max} \times Z_{max}) = (80 \times 40)$ . Other remarks are the same as in Figure 1.

Fig. 9 Time variations of (a) the magnetic field lines  $\mathbf{B} = (B_x, B_z)$ , (b) the velocity vector  $\mathbf{V} = (V_x, V_z)$ , (c) the density contours ( $\log \rho$ ) in model 5, where  $Z_{cor} = 12$  and other parameters are the same as in model 3. The total illustrated area is  $(X_{max} \times Z_{max}) = (80 \times 44)$ . Other remarks are the same as in Figure 1.

Fig. 10 The time evolution of the distributions in  $z$  of  $V_z$  at  $x = X_{max}/2$  (middle of the rising magnetic loop) for (a) model 5 ( $Z_{cor} = 12$ ; Fig. 9), (b) model 4 ( $Z_{cor} = 15$ ; Fig. 8), and (c) model 3 ( $Z_{cor} = 18$ ; Figs. 6 and 7). The dashed line in each figure indicates the height of the coronal base ( $=Z_{cor}$ ).

Fig. 11 The distributions in  $z$  of the initial gas pressure ( $p_g$ ) and the steady magnetic pressure ( $p_m$ ) for models 3, 4 and 5 at  $x = X_{max}/2$ . Note that  $p_m = B_x^2/8\pi \propto \Delta z^{-2}$  (cf. eq.[16]), and the proportional constant is the same as that of numerical results in Figure 7d.

Fig. 12 Illustration of the time evolution of the  $z$ -distribution of  $V_z$  for the quasi-1D self-similar solution in the case of  $a_1 = 0.06$  in equation (44).  $z_0$  is assumed to be  $4H$ . The shock-like front corresponds to the top of the

magnetic loop which is equivalent to the contact surface. (Here, it is assumed that there is a vacuum above the magnetic loop.) The unit of time is  $H/C_s$ .

Fig. 13 Illustration of the time evolution of the  $z$ -distribution of (a)  $\log \rho$  and (b)  $\log B_x$  for the quasi-1D self-similar solution in the case of  $a_1 = 0.06$  and  $N = 0.0$  in equation (45). Other remarks are the same as in Figure 11.

Fig. 14 Illustration of the time evolution of the  $z$ -distribution of (a)  $\log \rho$  and (b)  $\log B_x$  for the quasi-1D self-similar solution in the case of  $a_1 = 0.06$  and  $N = -0.5$  in equation (46). Other remarks are the same as in Figure 11.

Fig. A1 The linear growth rate ( $i\omega$ ) of the Parker instability of the gas layer considered in this paper as a function of the horizontal wavenumber  $k_x$ . Three cases  $\beta_* = 0.5, 1.0$ , and  $2.0$  are shown for  $k_y = 0$ .

Fig. A2 The  $z$ -distributions of the linear eigenfunction in the case of  $k_x = 0.314$  and  $k_y = 0$ . The magnitudes are normalized so that  $(i\bar{v}_x/C_s)_{max} = 1$ .

Tomoyuki Hanawa : Department of Physics, Faculty of Science, Nagoya University, Chikusa-ku, Nagoya 464, Japan

Toshiro Horiuchi and Ryoji Matsumoto: Department of Astronomy, Faculty of Science, University of Kyoto, Kyoto 606, Japan

Robert Rosner : Department of Astronomy and Astrophysics and Enrico Fermi Institute, University of Chicago, 5640 South Ellis Ave. Chicago, IL 60637

Kazunari Shibata : Department of Earth Sciences, Aichi University of Education, Kariya, Aichi 448, Japan

Toshiki Tajima : Department of Physics and Institute for Fusion Studies, University of Texas at Austin, Austin, TX 78712.

Yutaka Uchida : Department of Astronomy, University of Tokyo, Bunkyo-ku, Tokyo 113

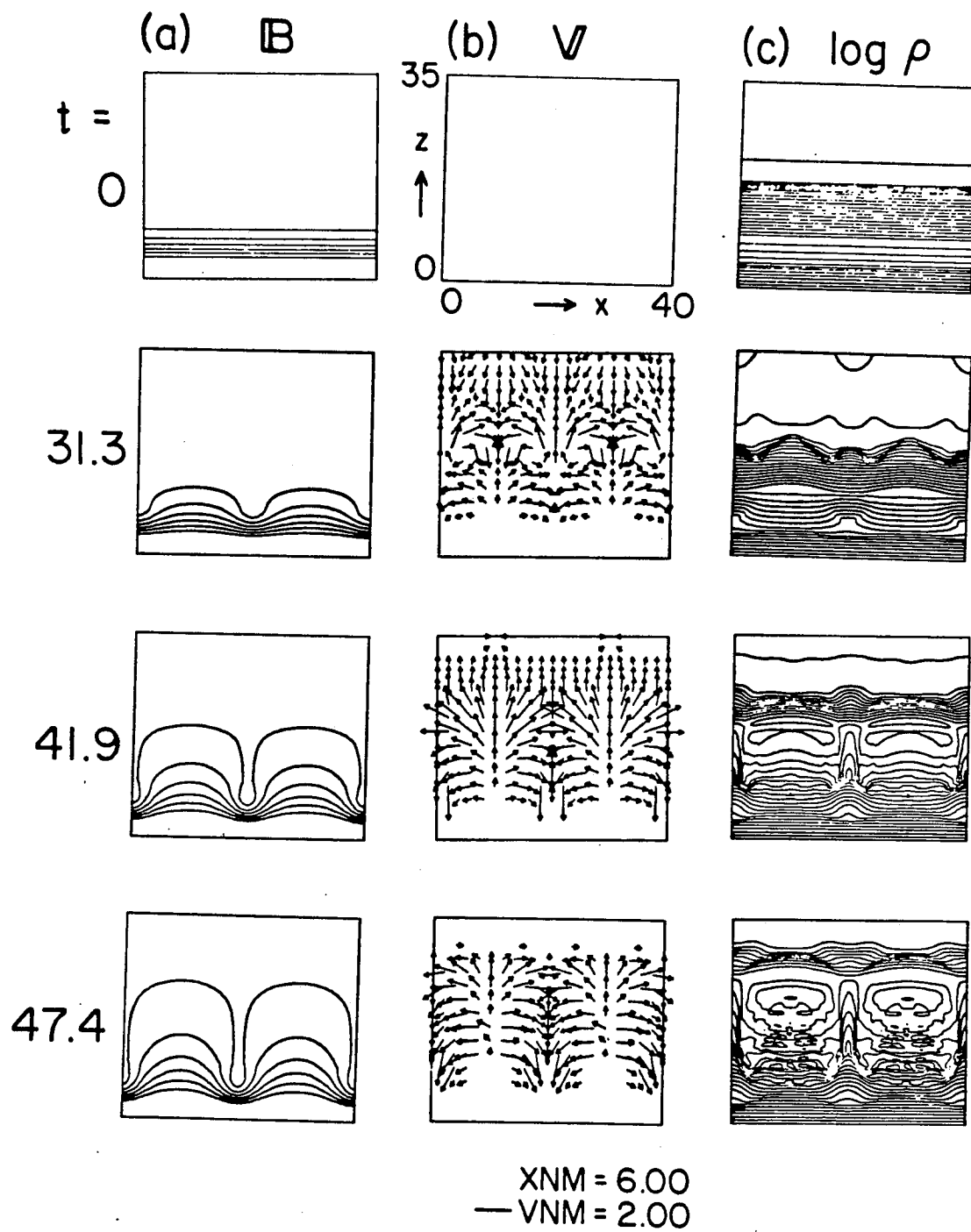


Fig. 1

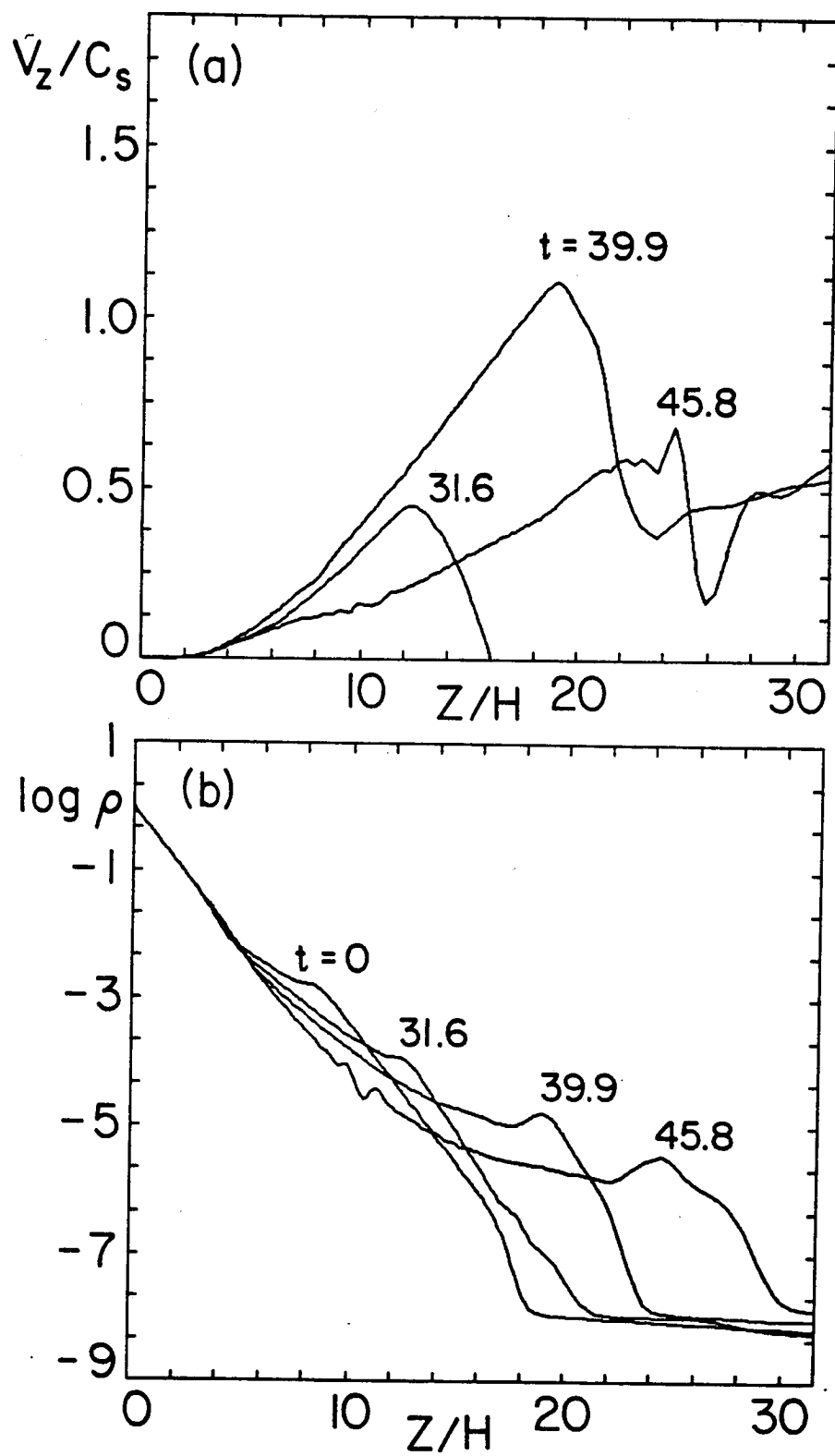


Fig. 2



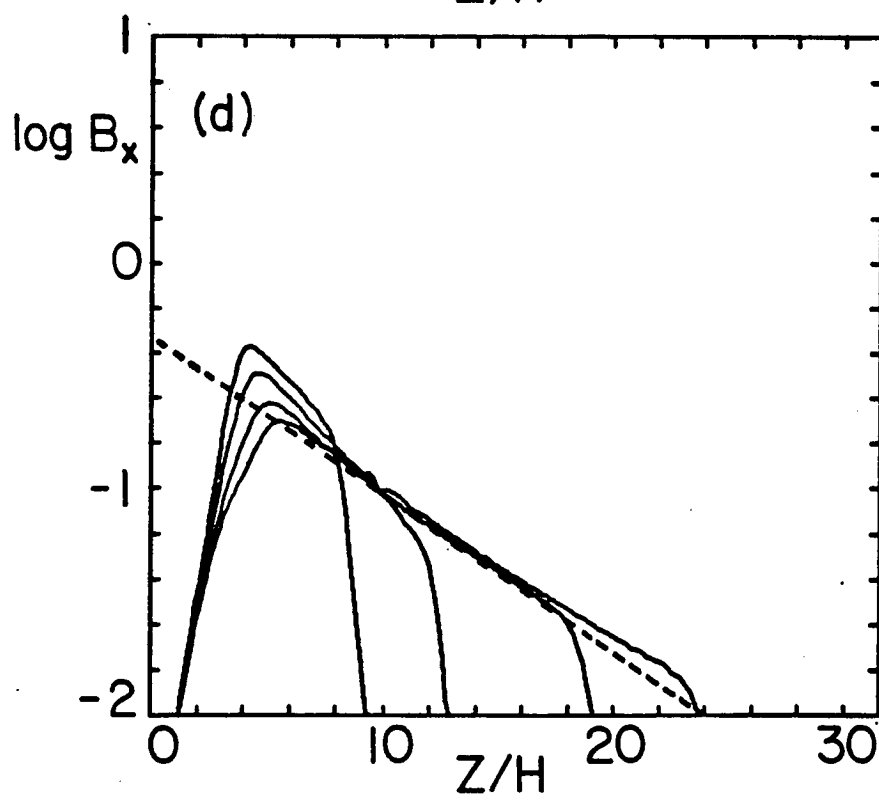
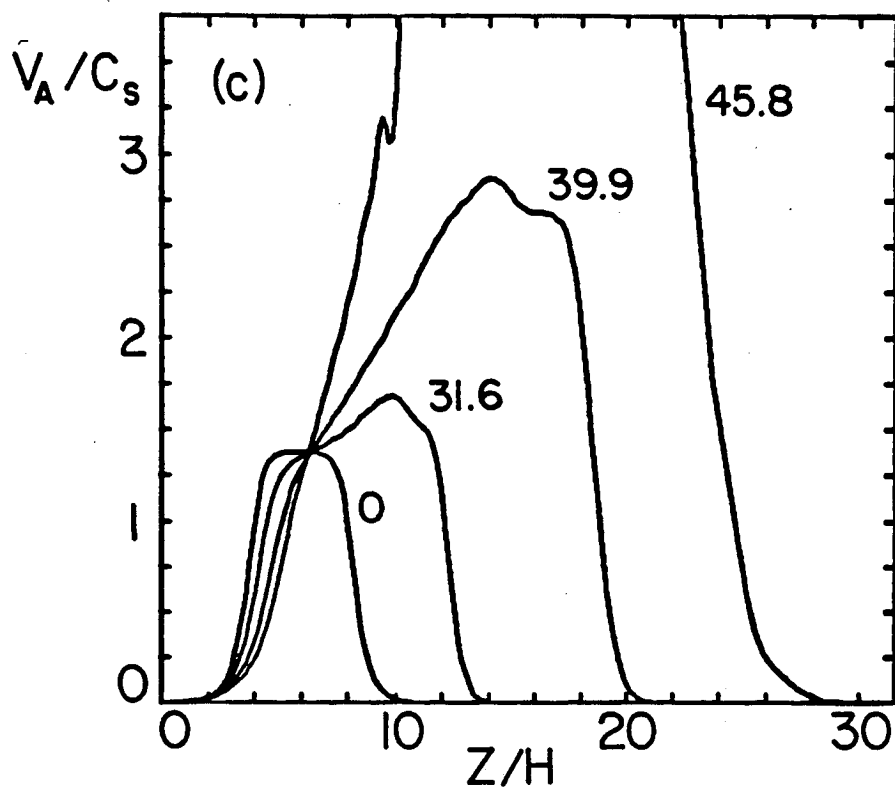


Fig. 2

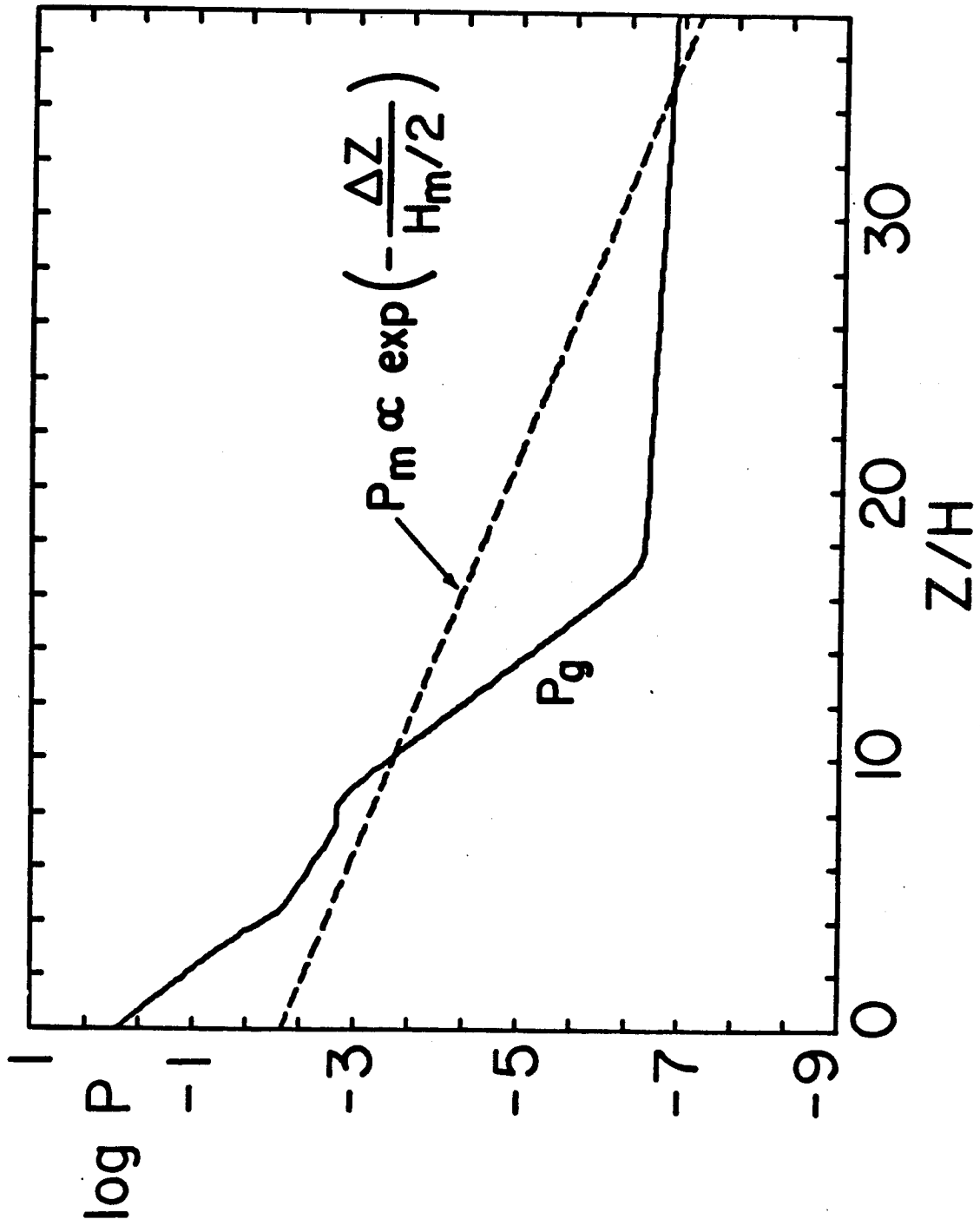


Fig. 3

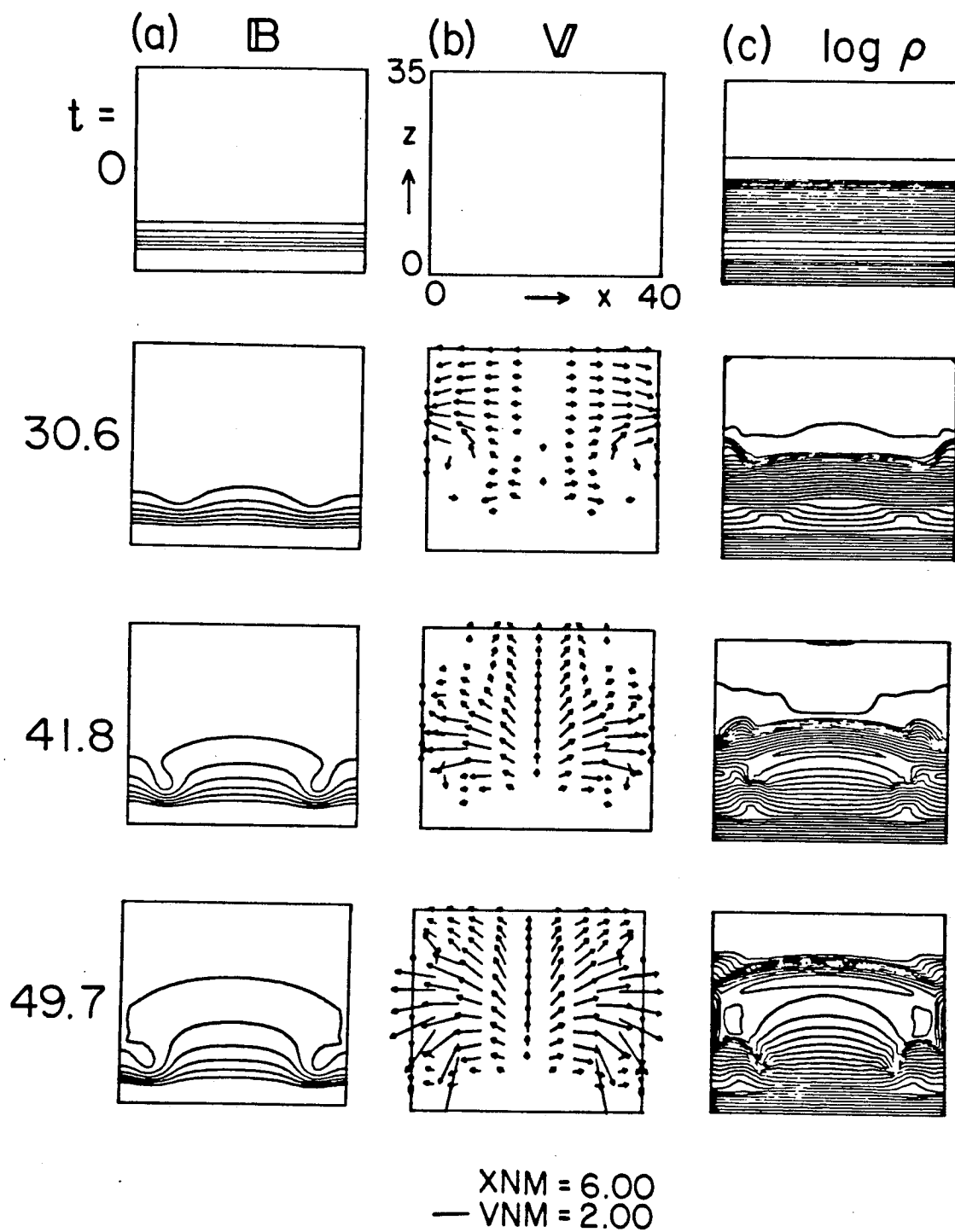


Fig. 4

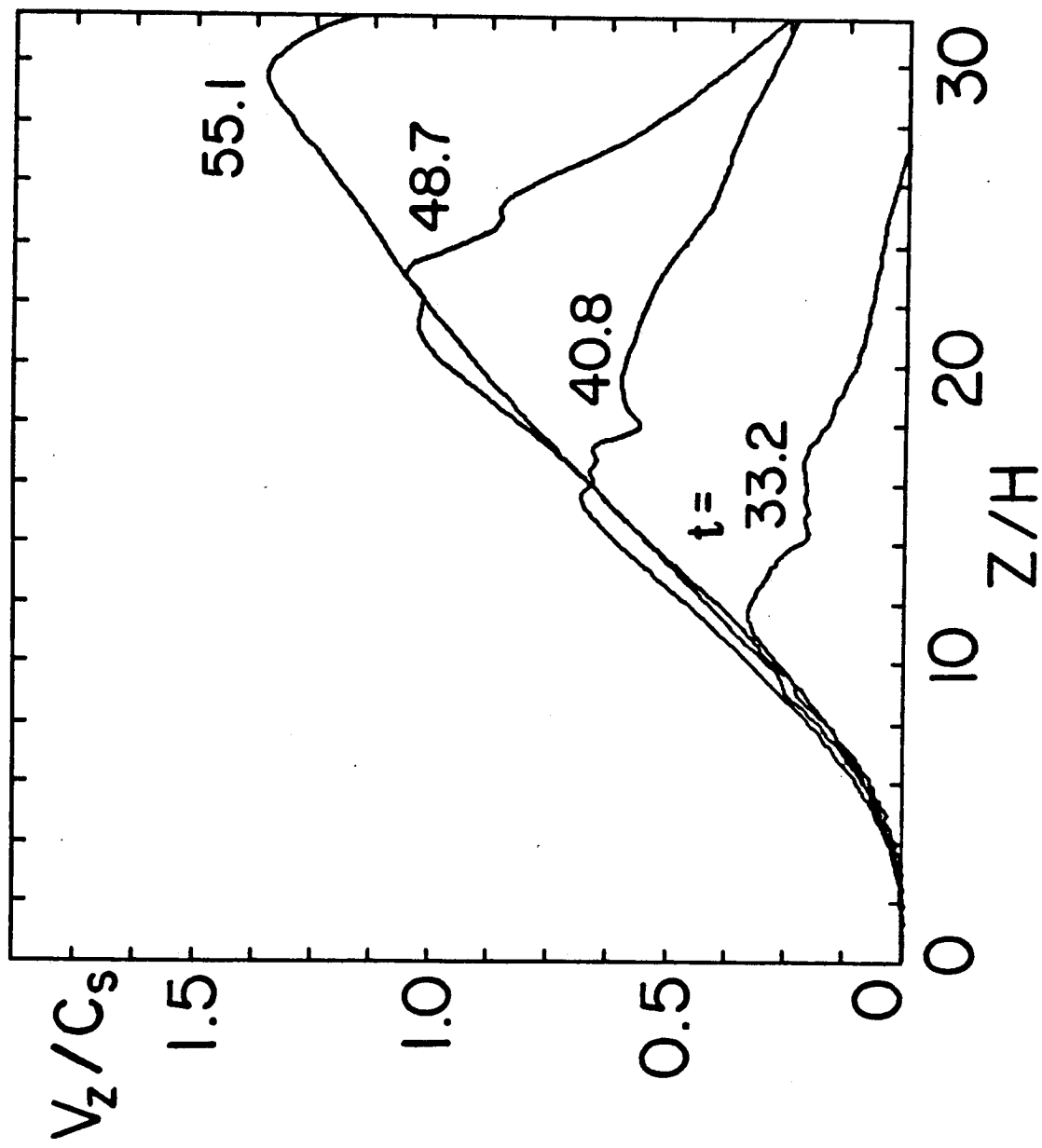


Fig. 5

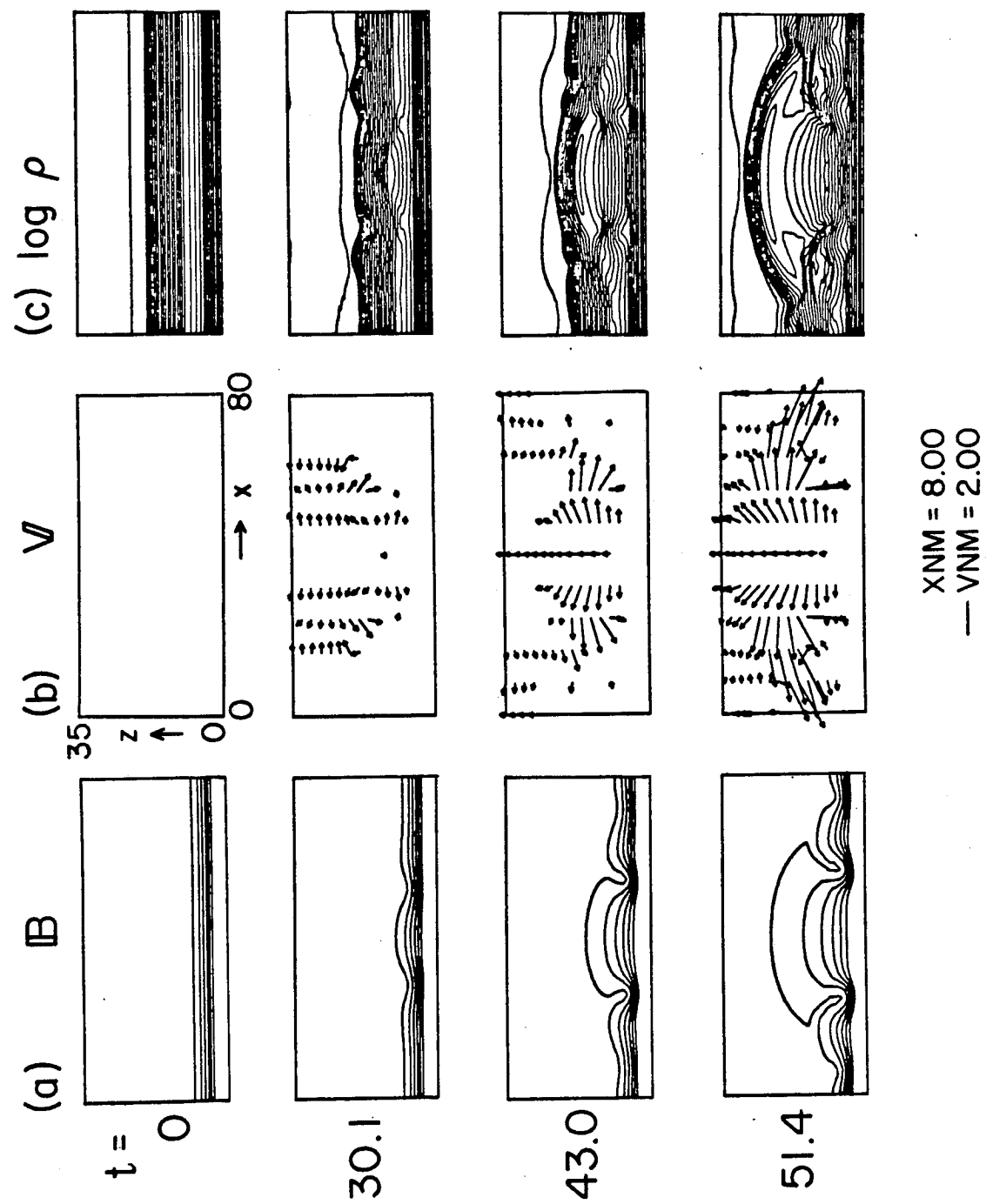


Fig. 6

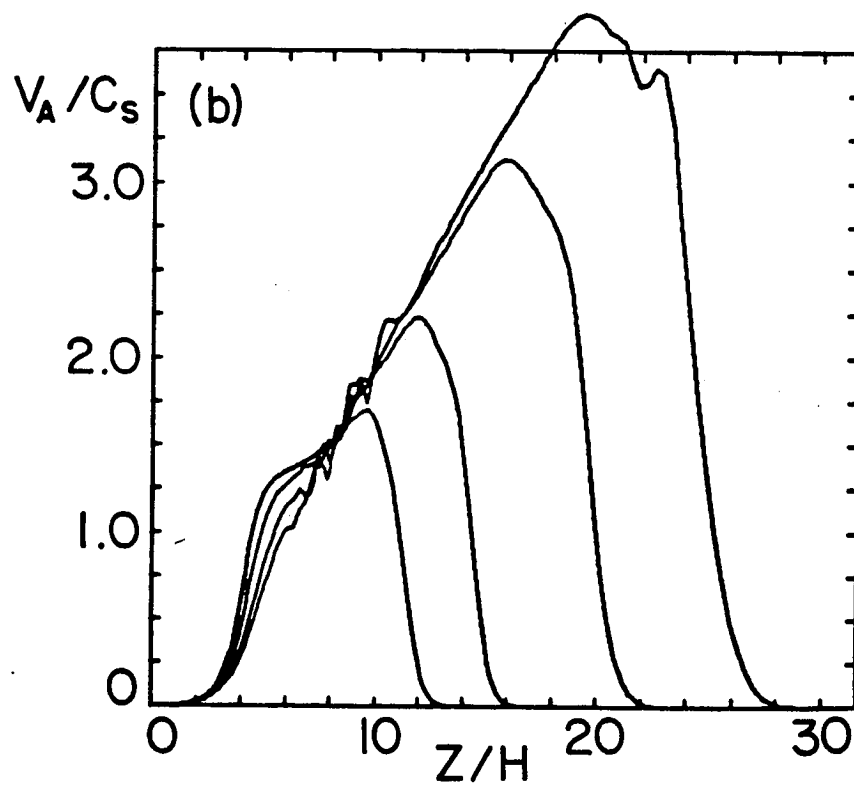
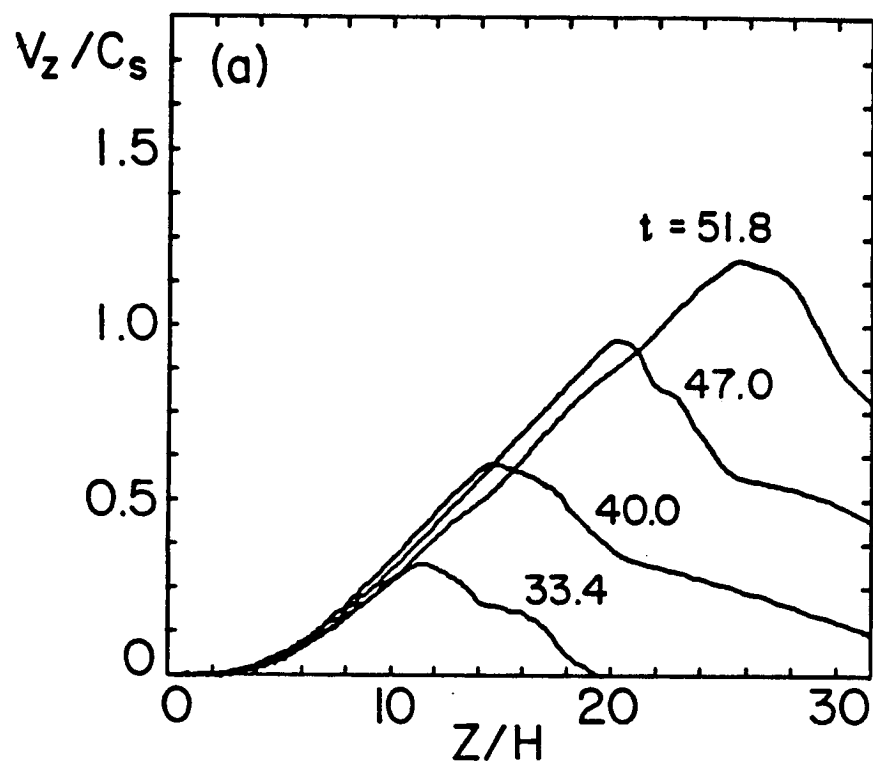


Fig. 7

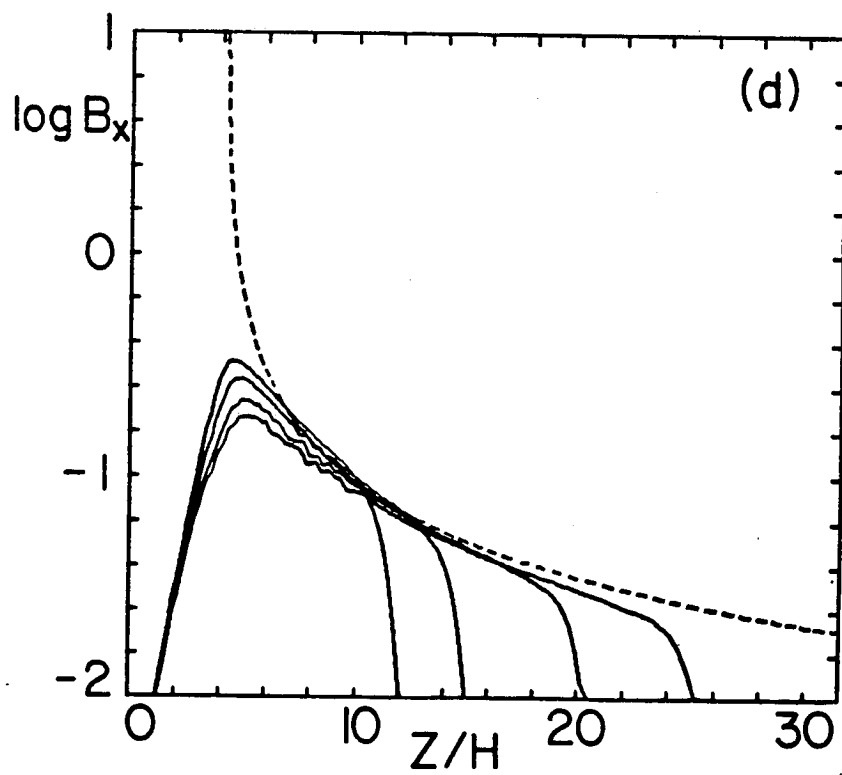
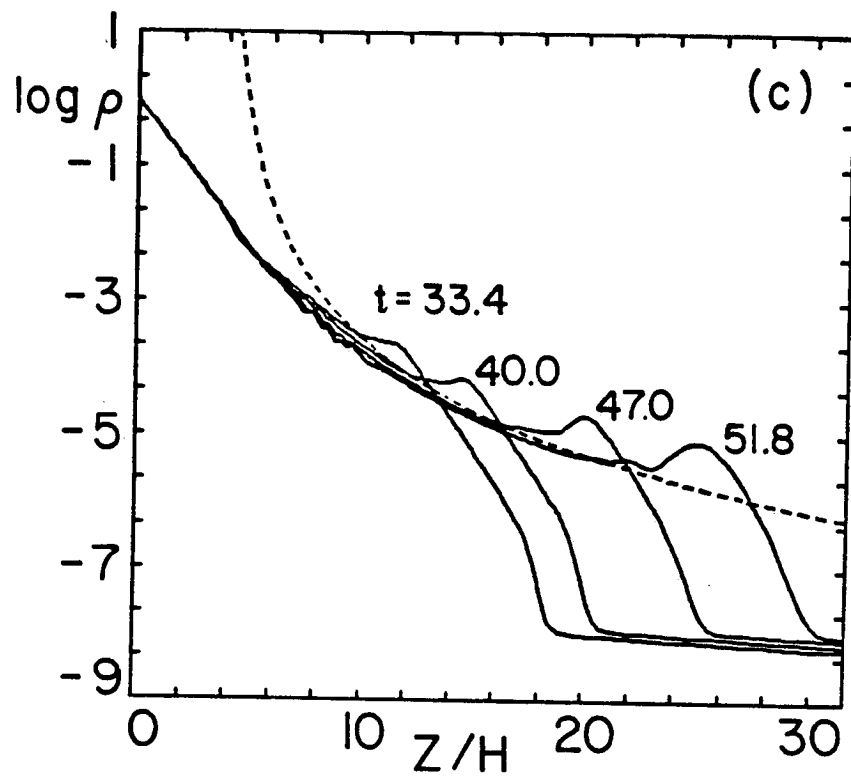


Fig. 7

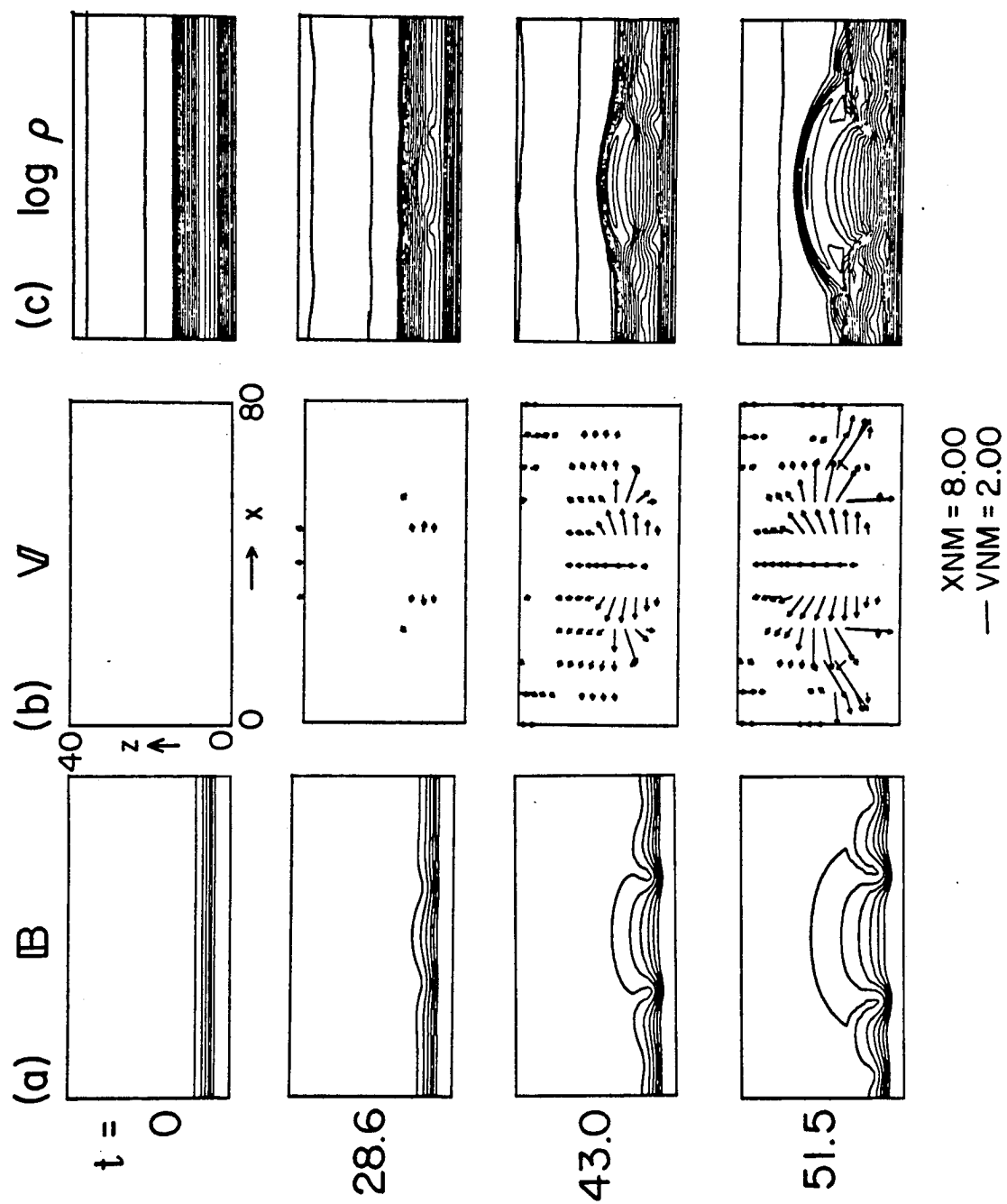


Fig. 8



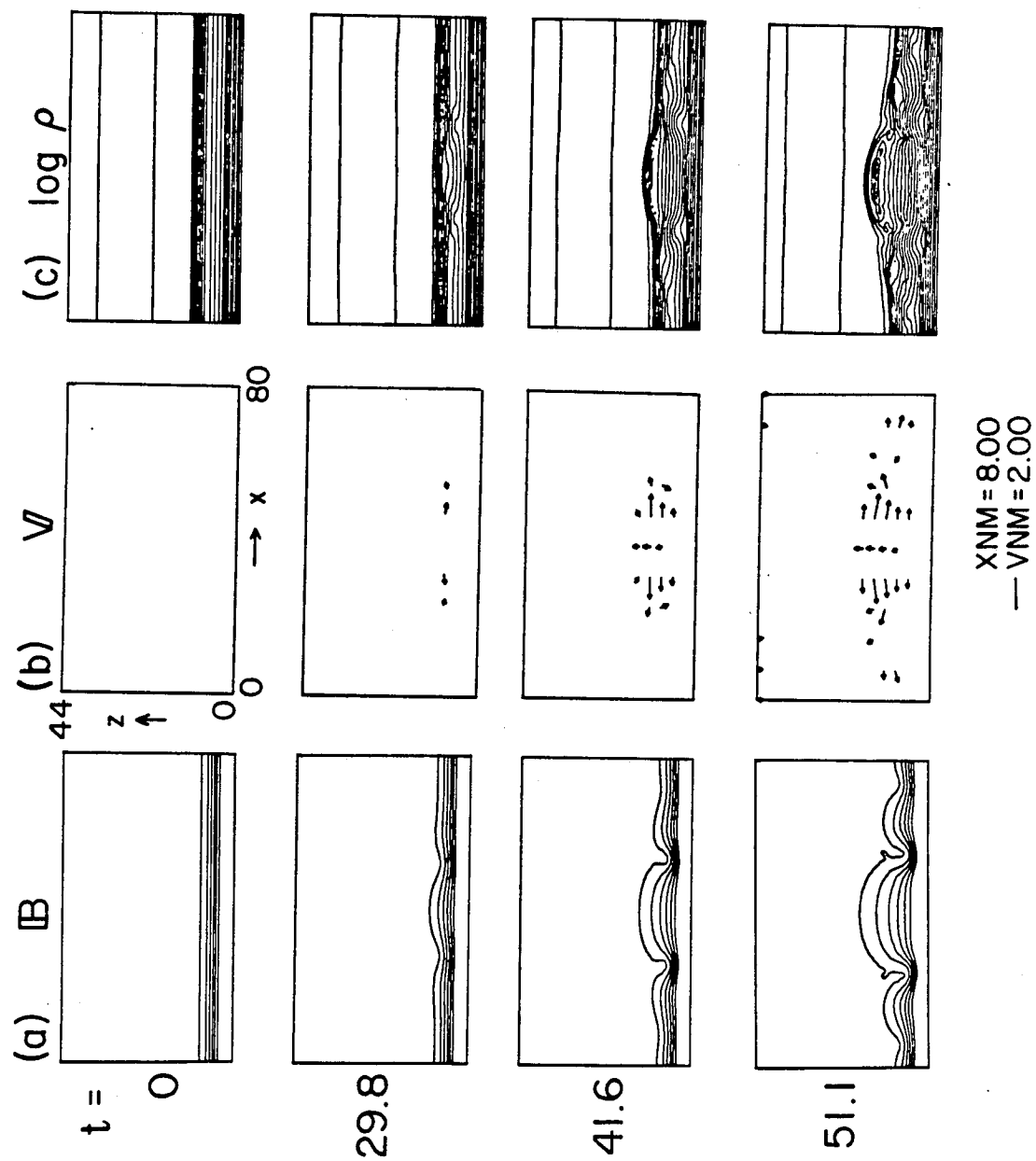


Fig. 9

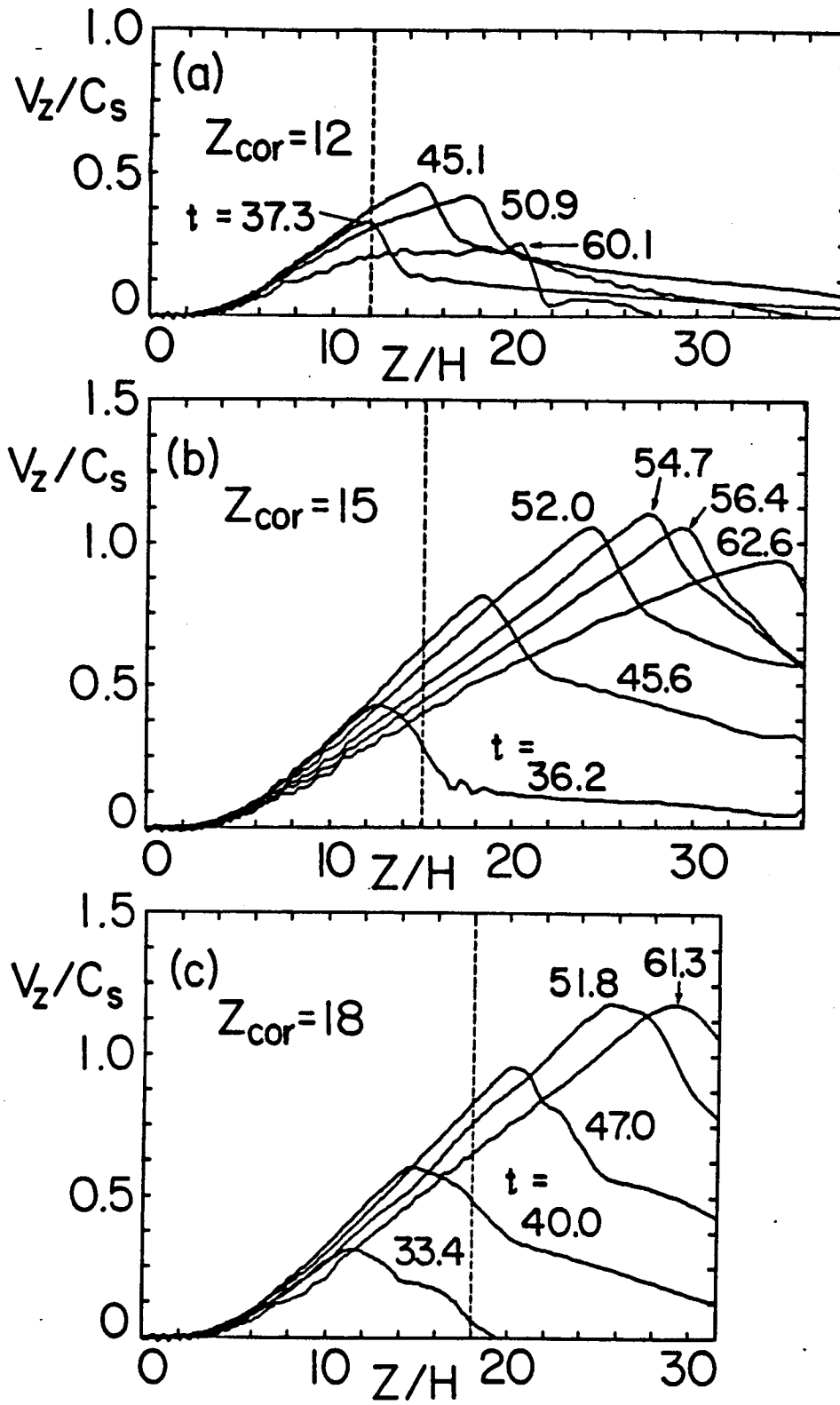


Fig. 10

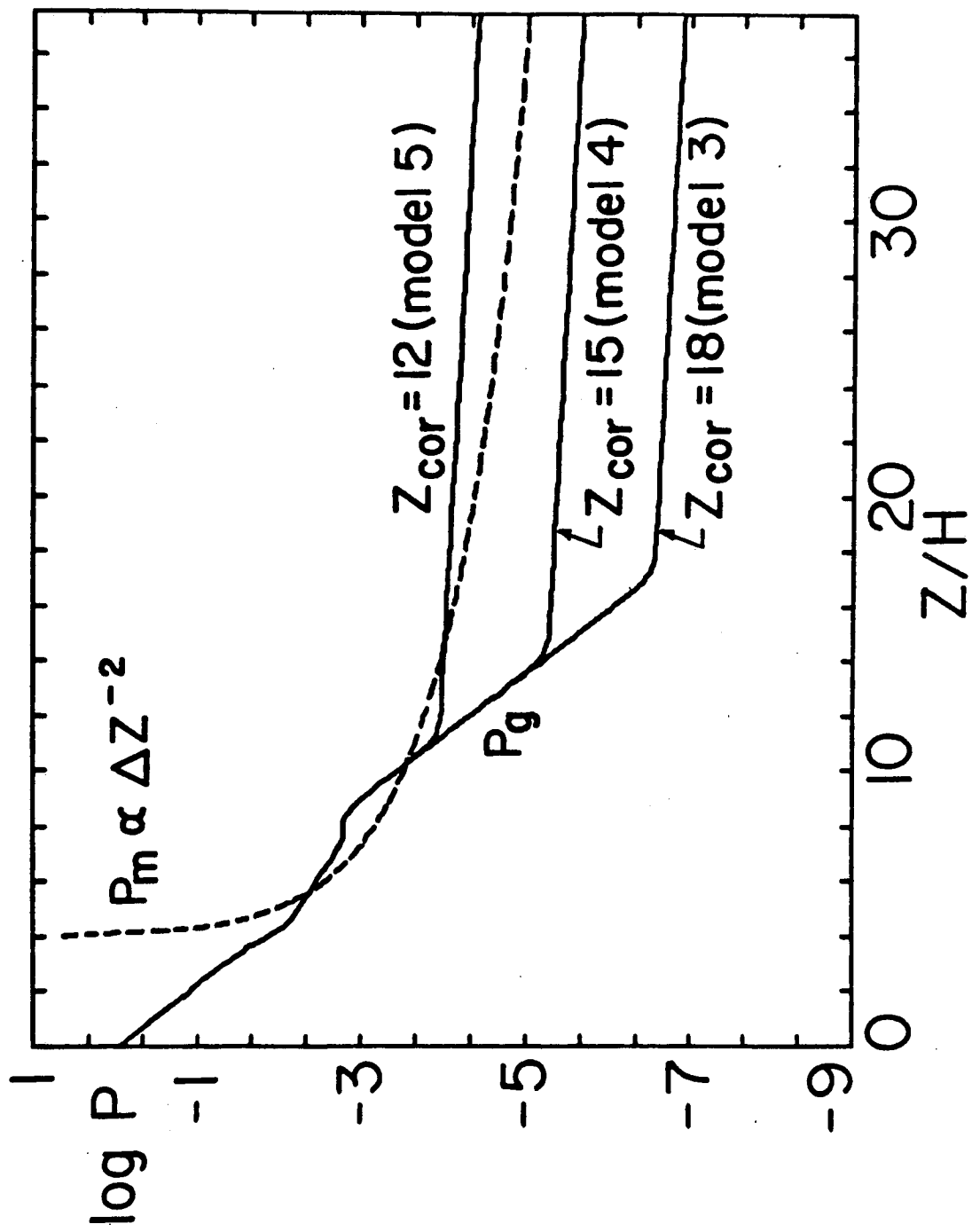


Fig. 11

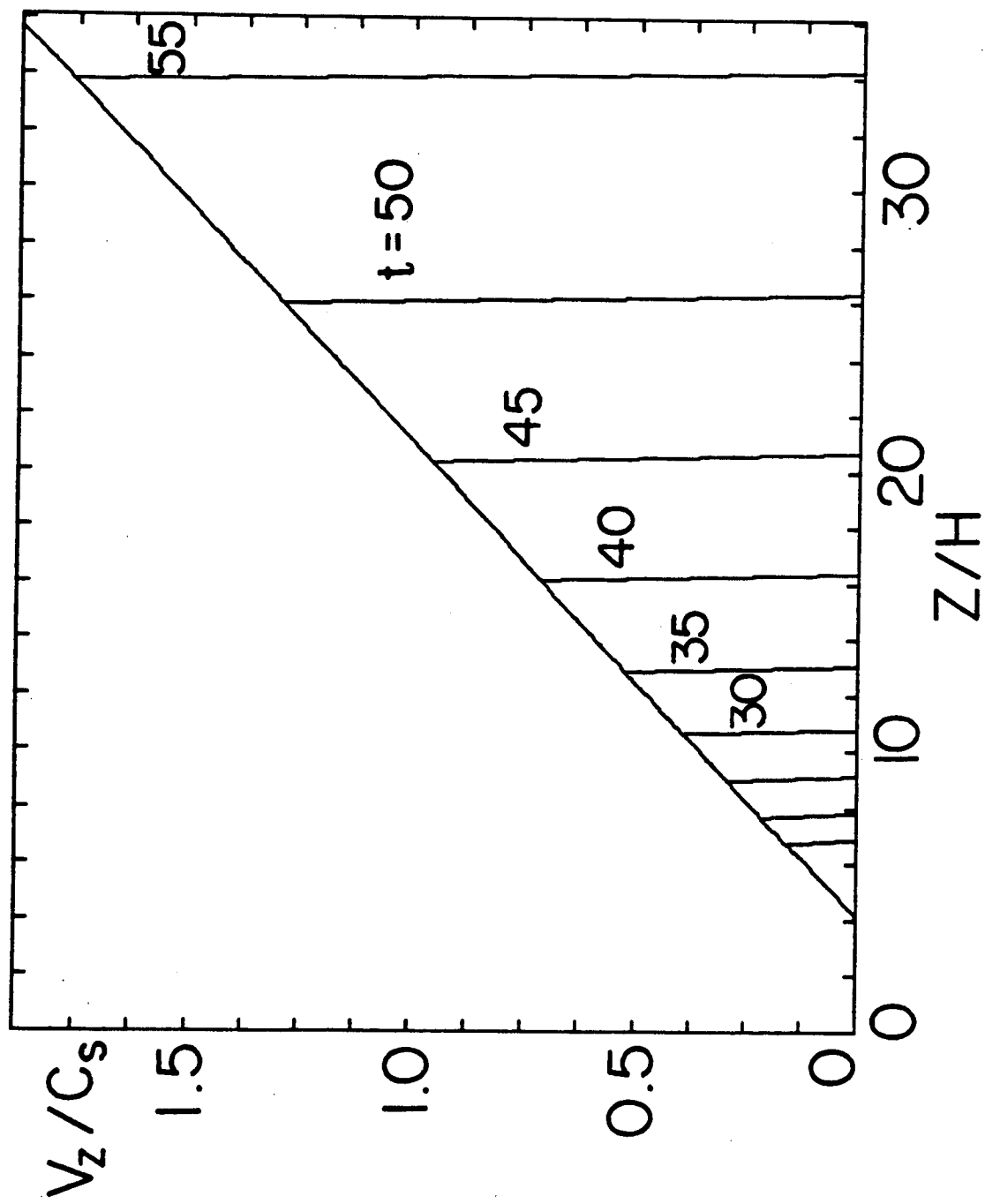


Fig. 12

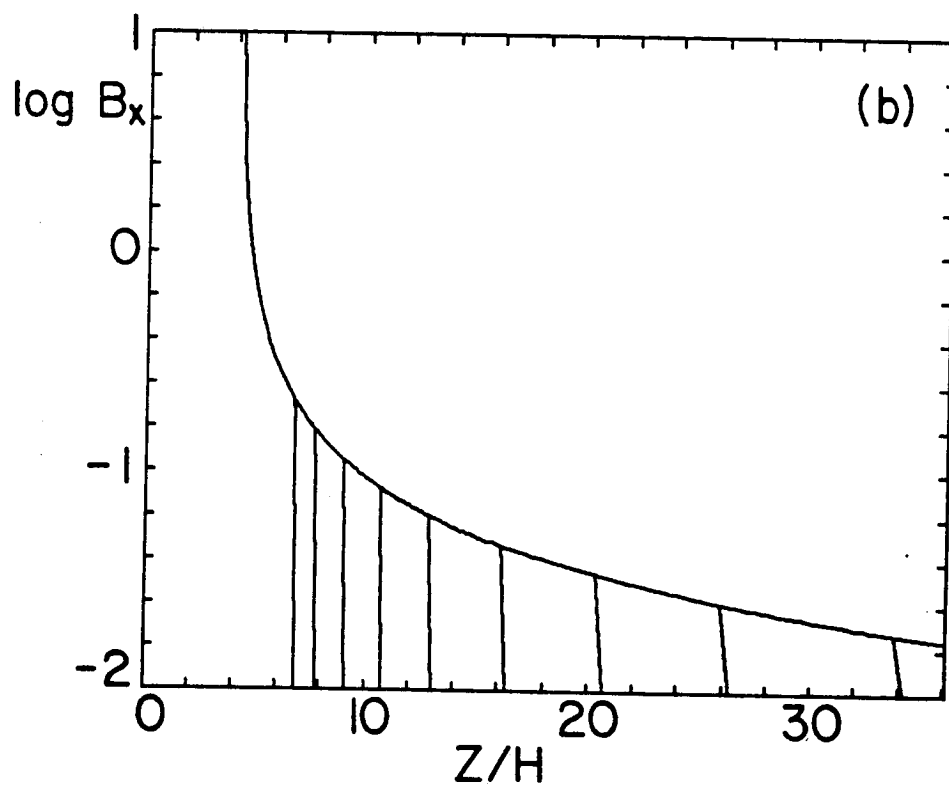
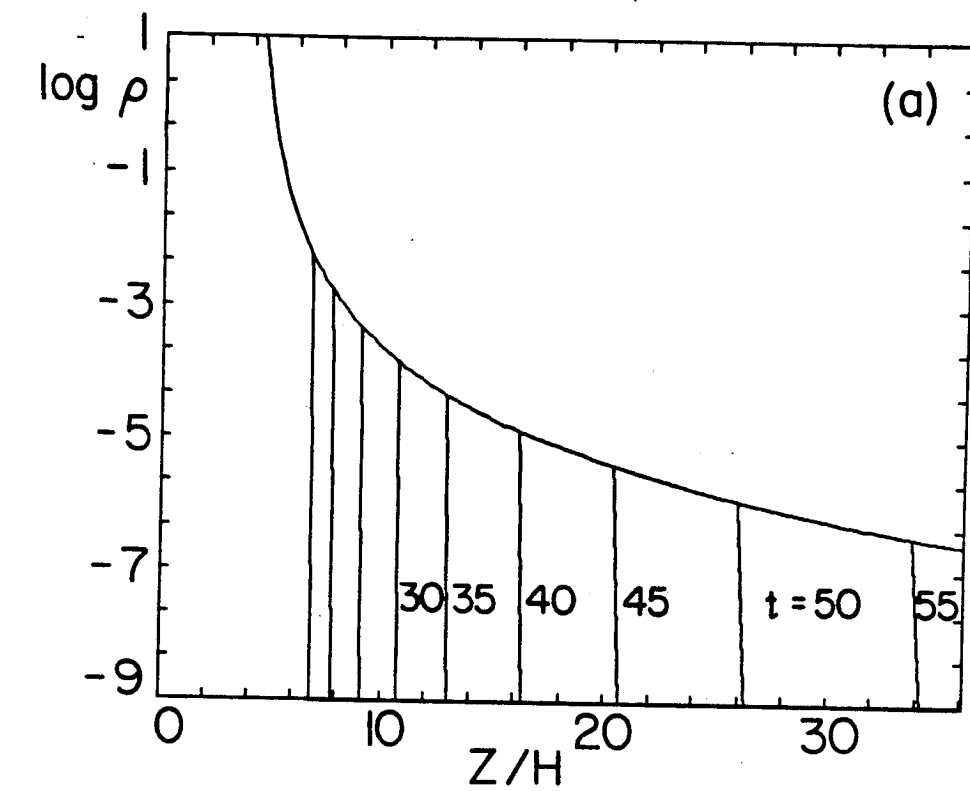


Fig. 13

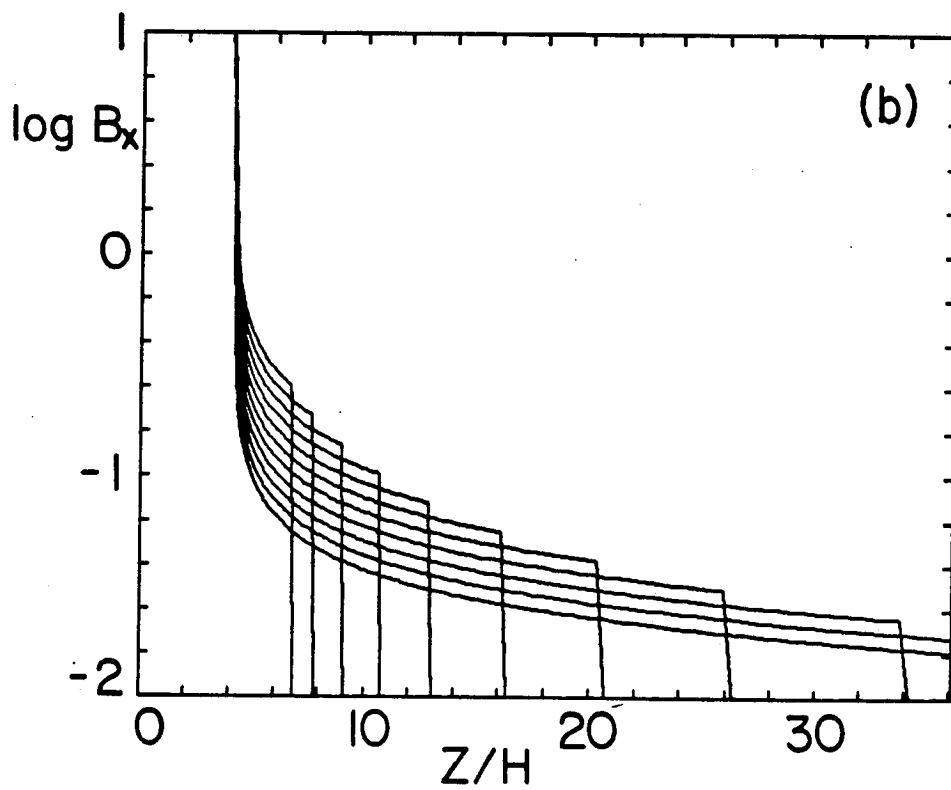
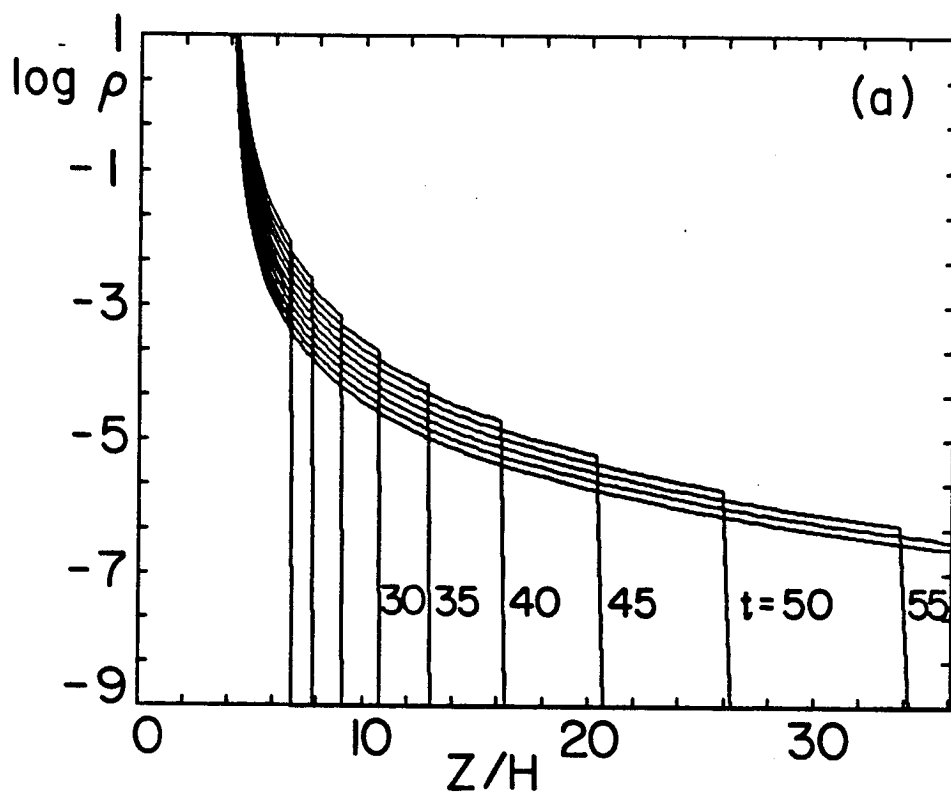


Fig. 14

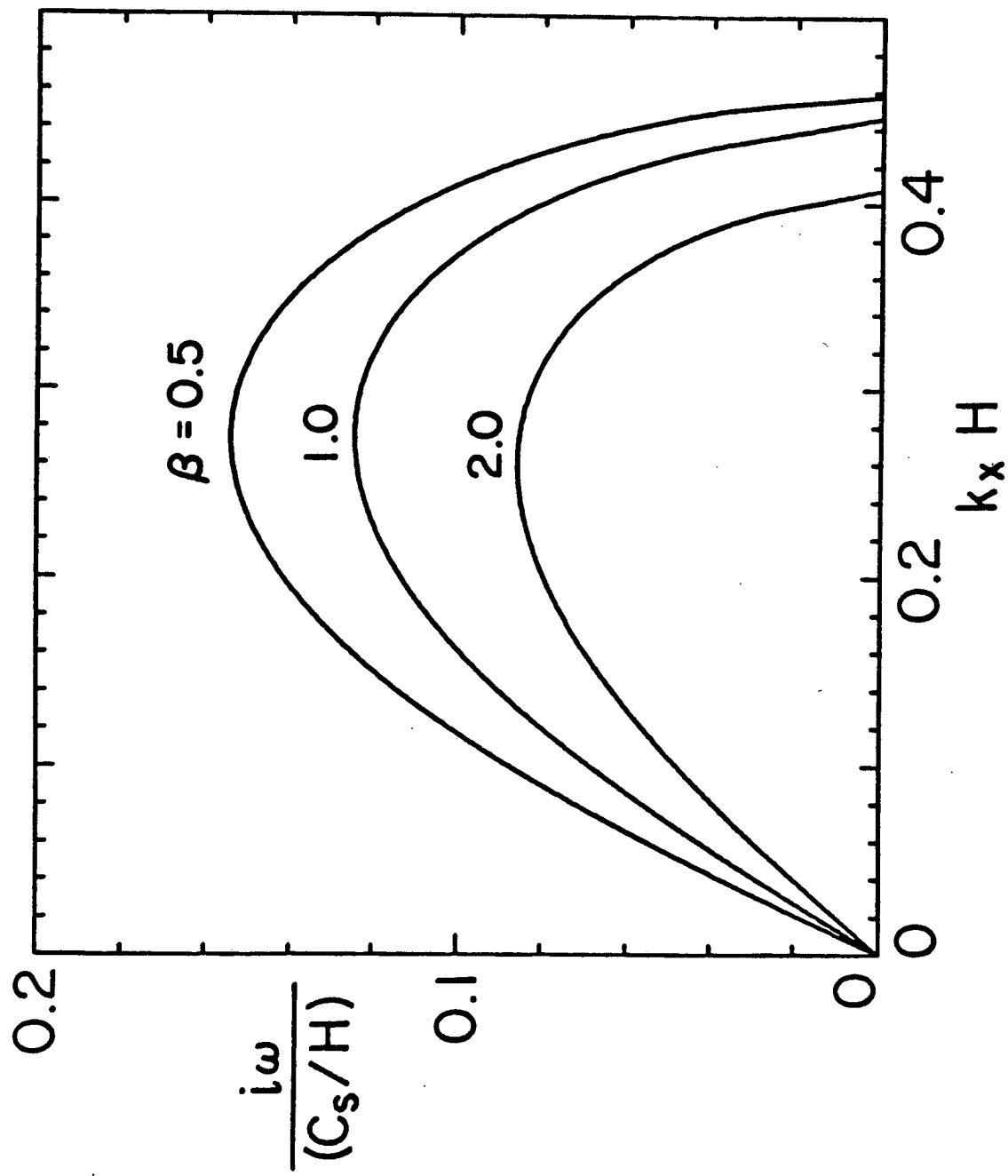


Fig. A1

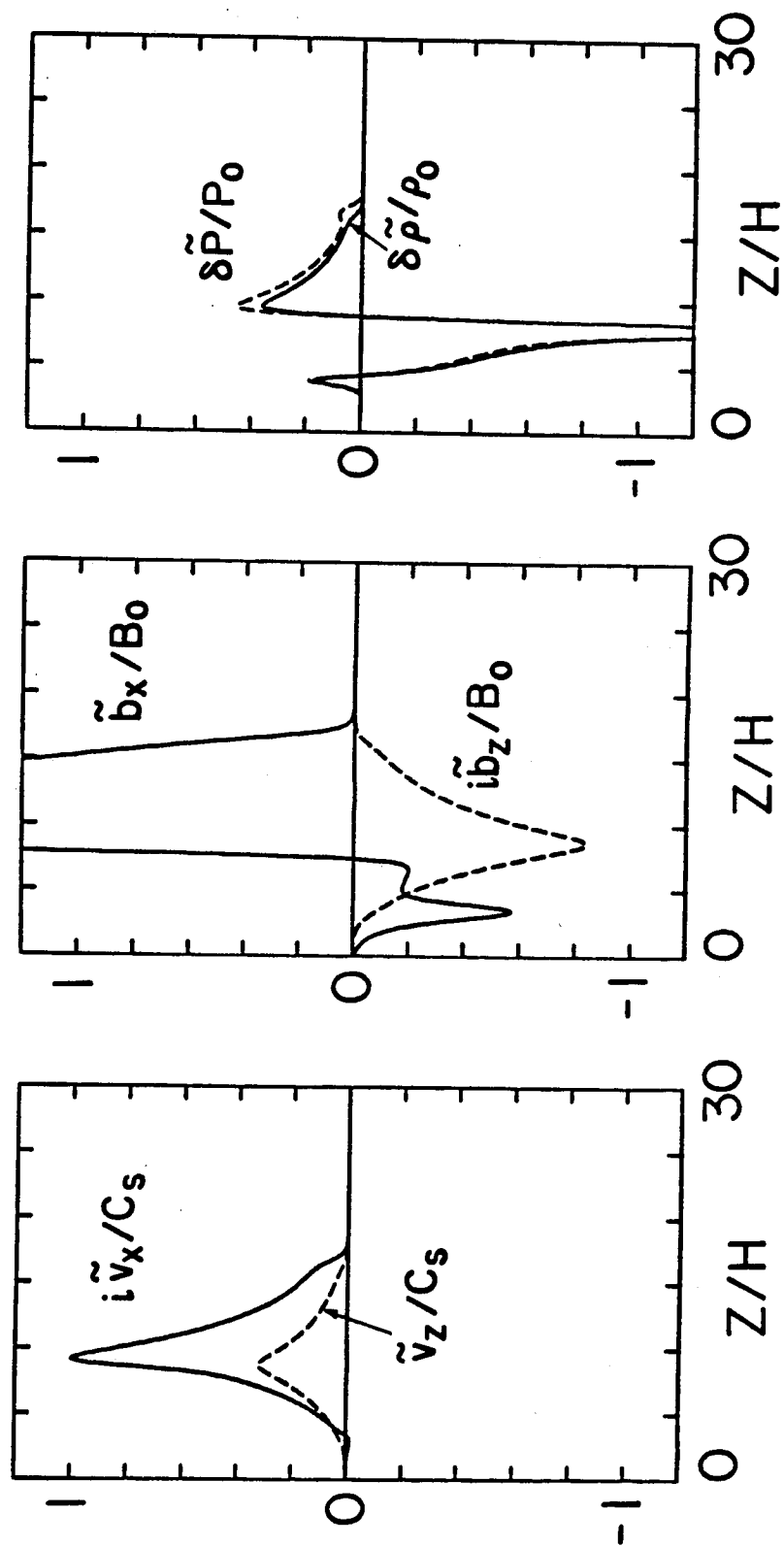


Fig. A2